Designing a retrievable and scalable cell encapsulation device for potential treatment of type 1 diabetes

Duo An[a], Alan Chiu[a], James A. Flanders[b], Wei Song[a], Dahua Shou[c], Yen-Chun Lu[a], Lars G. Grunnet[d], Louise Winkel[d], Camilla Ingvorsen[d], Nicolaj Strøyer Christophersen[d], Johannes Josef Fels[e], Fredrik Wolfhagen Sand[d], Yewei Ji[f], Ling Qi[f], Yehudah Pardo[g], Dan Luo[a,h,i], Meredith Silberstein[j], Jintu Fan[c], and Minglin Ma[a,1]

[a]Department of Biological and Environmental Engineering, Cornell University, Ithaca, NY 14853; [b]Department of Clinical Sciences, Cornell University, Ithaca, NY 14853; [c]Department of Fiber Science and Apparel Design, Cornell University, Ithaca, NY 14853; [d]Diabetes and Cardiovascular Disease, Novo Nordisk A/S, 2760 Måløv, Denmark; [e]Research Bioanalysis, Novo Nordisk A/S, 2760 Måløv, Denmark; [f]Department of Molecular and Integrative Physiology, University of Michigan Medical School, Ann Arbor, MI 48105; [g]Meinig School of Biomedical Engineering, Cornell University, Ithaca, NY 14853; [h]Kavli Institute at Cornell for Nanoscale Science, Cornell University, Ithaca, NY 14853; [i]Suzhou Institute of Nano-Tech and Nano-Bionics, Chinese Academy of Sciences, Suzhou 215123, People's Republic of China; and [j]Sibley School of Mechanical and Aerospace Engineering, Cornell University, Ithaca, NY 14853

Edited by Kristi S. Anseth, University of Colorado, Boulder, Boulder, CO, and approved December 1, 2017 (received for review May 26, 2017)

Cell encapsulation has been shown to hold promise for effective, long-term treatment of type 1 diabetes (T1D). However, challenges remain for its clinical applications. For example, there is an unmet need for an encapsulation system that is capable of delivering sufficient cell mass while still allowing convenient retrieval or replacement. Here, we report a simple cell encapsulation design that is readily scalable and conveniently retrievable. The key to this design was to engineer a highly wettable, Ca^{2+}-releasing nanoporous polymer thread that promoted uniform in situ cross-linking and strong adhesion of a thin layer of alginate hydrogel around the thread. The device provided immunoprotection of rat islets in immunocompetent C57BL/6 mice in a short-term (1-mo) study, similar to neat alginate fibers. However, the mechanical property of the device, critical for handling and retrieval, was much more robust than the neat alginate fibers due to the reinforcement of the central thread. It also had facile mass transfer due to the short diffusion distance. We demonstrated the therapeutic potential of the device through the correction of chemically induced diabetes in C57BL/6 mice using rat islets for 3 mo as well as in immunodeficient SCID-Beige mice using human islets for 4 mo. We further showed, as a proof of concept, the scalability and retrievability in dogs. After 1 mo of implantation in dogs, the device could be rapidly retrieved through a minimally invasive laparoscopic procedure. This encapsulation device may contribute to a cellular therapy for T1D because of its retrievability and scale-up potential.

cell encapsulation | diabetes | medical device | cell transplantation | retrievable

Type 1 diabetes (T1D) is an autoimmune disease where the patients' insulin-producing pancreatic islet cells are mistakenly destroyed by their own immune system (1). Although current treatment by daily injections or infusion of exogenous insulin provides blood glucose (BG) control, the approach requires constant attention and strict compliance. It does not cure the disease or prevent the many devastating effects associated with diabetes, such as blindness, hypertension, kidney disease, and vasculitis (2). Islet transplantation provides a potential alternative to treat T1D and has been shown to restore normoglycemia (3). However, to avoid immune rejection of transplanted islets, long-term immunosuppressive drug administration is necessary, which is known to cause deleterious side effects (4).

Cell encapsulation allows transplantation of islets or stem cell-derived beta-like cells without immunosuppression and has therefore become a very promising approach for T1D treatment (5–12). The encapsulating material or device protects the cells from the host immune rejection while simultaneously allowing mass transfer to maintain cell survival and function. Despite tremendous research efforts worldwide and much significant progress that has been made, clinical application of cell encapsulation has remained elusive (5, 8, 12). Currently there are two major types of islet encapsulation systems: macroscopic devices and hydrogel microcapsules. Both systems have been shown to be functional in numerous preclinical studies but unfortunately have had serious limitations for clinical applications. For example, macroscopic devices such as diffusion chambers have a small surface area for mass transfer and consequently low encapsulation capacity (8–10, 13, 14). Even though the capacity problem may be addressed by increasing the cell packing density, dense packing will also inevitably lead to a hypoxic environment and associated impairment in insulin secretion (15, 16). Thus, the scale-up to a capacity sufficient to cure a human patient has been challenging (5, 8–10, 14, 17, 18). Alginate hydrogel capsules, on the other hand, have a large surface area for mass transfer and can, in principle, deliver a sufficient number of islets (19–24). In particular, the biocompatibility of alginate materials has been significantly improved in recent years through advanced purifications, formulations, and chemical modifications (7, 11, 25–31). However, one major problem with capsules is that it is almost impossible to completely retrieve or replace them after implantation in the peritoneal cavity due to the complicated organ structures and the large capsule number required (i.e., ∼100,000 capsules needed for a human patient) (4, 8, 18, 32). This raises significant risks and concerns in

Significance

Cell encapsulation holds great potential as a better treatment for type 1 diabetes. An encapsulation system that is scalable to a clinically relevant capacity and can be retrieved or replaced whenever needed is highly desirable for clinical applications. Here we report a cell encapsulation device that is readily scalable and conveniently retrievable through a minimally invasive laparoscopic procedure. We demonstrated its mechanical robustness and facile mass transfer as well as its durable function in diabetic mice. We further showed, as a proof of concept, its scalability and retrievability in dogs. We believe this encapsulation device may contribute to a cellular therapy for type 1 diabetes and potentially other endocrine disorders and hormone-deficient diseases.

Author contributions: D.A., A.C., and M.M. designed research; D.A., A.C., J.A.F., W.S., D.S., Y.-C.L., L.G.G., L.W., C.I., N.S.C., J.J.F., F.W.S., Y.J., and M.S. performed research; D.A. and M.M. contributed new reagents/analytic tools; D.A., A.C., J.A.F., W.S., D.S., Y.-C.L., L.G.G., L.W., C.I., N.S.C., J.J.F., F.W.S., Y.J., L.Q., Y.P., D.L., M.S., J.F., and M.M. analyzed data; and D.A., J.A.F., Y.P., M.S., and M.M. wrote the paper.

Conflict of interest statement: L.G.G., L.W., C.I., N.S.C., J.J.F., and F.W.S. are Novo Nordisk A/S employees and are shareholders in the company.

This article is a PNAS Direct Submission.

[1]To whom correspondence should be addressed. Email: mm826@cornell.edu.

This article contains supporting information online at www.pnas.org/lookup/suppl/doi:10.1073/pnas.1708806115/-/DCSupplemental.

the event of transplant failure or medical complications (5, 8, 12, 33, 34). Retrievability is also an important issue associated with the regulatory approval process (35).

To address these challenges, here we report a simple and translatable cell encapsulation design that is both scalable and retrievable. The design involves a one-step in situ cross-linking of an alginate hydrogel around a nanoporous, wettable, Ca^{2+}-releasing polymer thread. We term the design as TRAFFIC (thread-reinforced alginate fiber for islets encapsulation). In TRAFFIC, the hydrogel encapsulating cells provide the necessary mass transfer and biocompatibility similar to conventional hydrogel capsules, while the polymer thread imparts mechanical strength and enables easy handling, implantation, and retrieval. The device may be extended to meters long and still be entirely retrievable through a minimally invasive laparoscopic procedure. To demonstrate the therapeutic potential of the device, we encapsulated and transplanted rat islets into diabetic C57BL/6 mice or human islets into SCID-Beige mice and obtained diabetes correction for up to several months. As a proof of concept, we scaled up the device and showed its retrievability in dogs. Given its simplicity and translatability, this device may contribute significantly to a cell encapsulation therapy for T1D and potentially many other diseases.

Design and Fabrication of the Device

The TRAFFIC device consists of a tough polymer thread and a uniform, strongly adhered alginate hydrogel layer with controllable thickness (Fig. 1*A*). To obtain strong adhesion between the thread and the hydrogel, we designed the thread by mimicking the highly adhesive, nanoporous silks that certain spiders use for capillary-enabled water collection and retention (36). To achieve uniform, controllable hydrogel formation, we incorporated a Ca^{2+}-releasing mechanism into the thread design. The fabrication process (Fig. 1*B*) is simple but involves several material design principles. First, to create the spider silk-like, nanoporous (and mechanically tough) thread, we chose to coat a nylon suture with 7% (wt/vol) poly(methyl methacrylate)/N,*N*-dimethylformamide (PMMA/DMF) solution. Under humid conditions, the drying of the polymer solution resulted in evaporative cooling and phase separation, leading to nanoporous structures (37, 38). However, due to the surface tension-driven Rayleigh Instability (39, 40), the coating solution dewetted on the suture and formed patchy beads instead of continuous coatings (Fig. 1*C* and *SI Appendix*, SI-1), leading to a "beads-on-a-string" morphology after drying. To overcome this problem, we twisted two sutures (typically 5–0) together to form a double helix and folded the helix in the middle. Upon folding, the torsion generated from the twisting spontaneously led to a stable

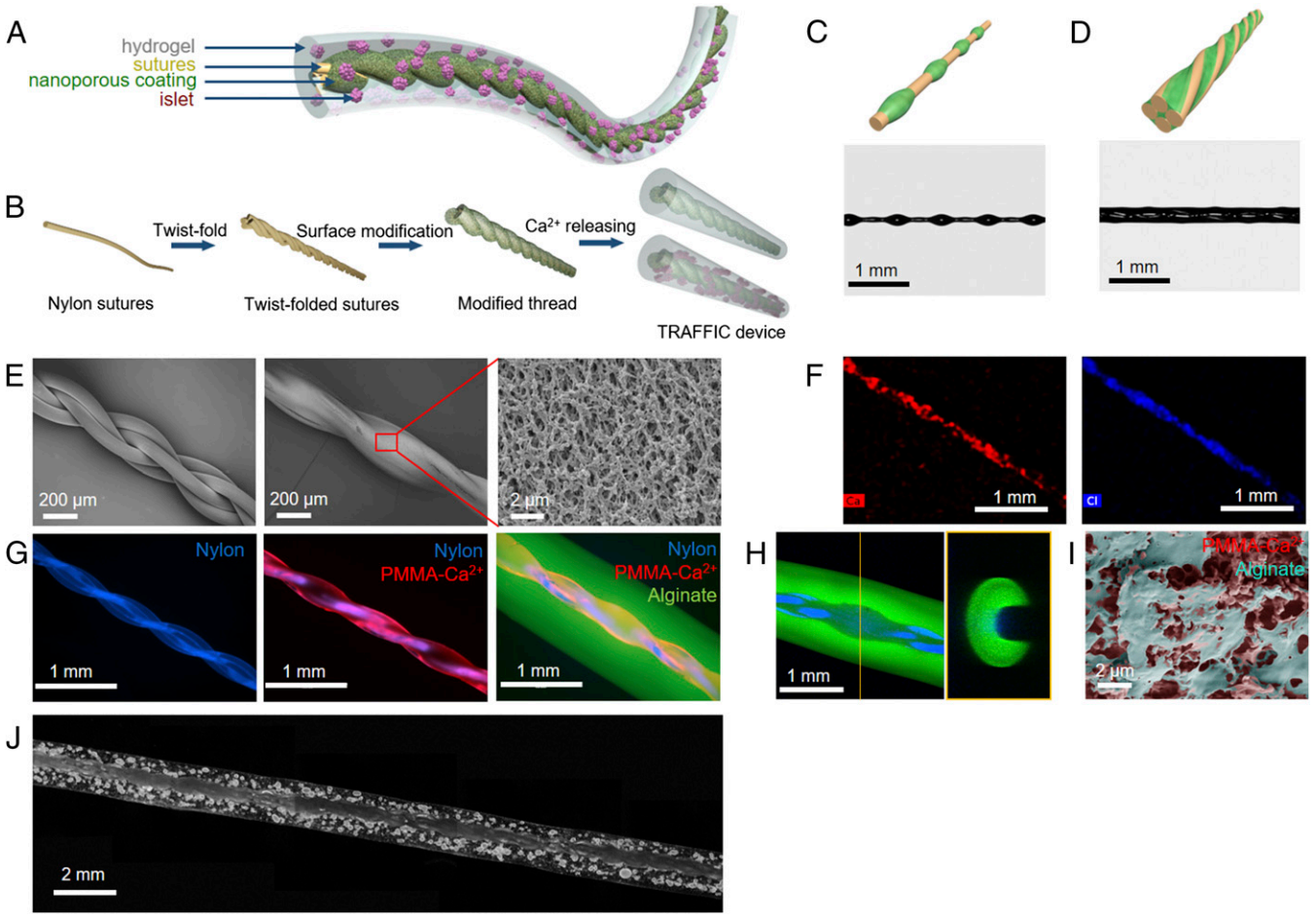

Fig. 1. Schematics and fabrication of the TRAFFIC device. (*A*) Schematic illustration of the design of TRAFFIC. (*B*) Schematic illustration of the fabrication process. (*C* and *D*) Schematic illustrations and optical images of the PMMA/$CaCl_2$/DMF solution coating on a monofilament nylon suture (*C*) and a thread made of twist-folded sutures (*D*). (*E*) SEM images of the thread and the uniform nanoporous surface modifications. (*F*) EDS element mapping of Ca and Cl on a modified thread. (*G*) Fluorescent microscopic images of the thread, modified thread, and a TRAFFIC device (without cells). (*H*) Confocal images of a TRAFFIC device. (*I*) An SEM image of the interface between alginate hydrogel and the modified thread after lyophilization. (*J*) A composite microscopic image (stitched from three individual microscopic images of 2× magnification) of a TRAFFIC device encapsulating rat islets.

four-strand thread with a "ridges-in-grooves" structure (Fig. 1 *D* and *E* and *SI Appendix*, SI-2). In contrast to the coating on the smooth suture, the solution formed liquid wedges along the grooves of the twist-folded, four-strand thread. This simple method prevented the dewetting and resulted in a continuous nanoporous coating (Fig. 1 *D* and *E* and *SI Appendix*, SI-2) on the thread. Lastly, within the nanoporous coating, we incorporated the cross-linking agent $CaCl_2$ by taking advantage of an unusual and unique property of $CaCl_2$—its solubility in DMF. By dissolving 2.5% (wt/vol) $CaCl_2$ in the PMMA/DMF coating solution, we obtained a nanoporous thread with a uniform distribution of Ca and Cl as evidenced by energy dispersive spectrometer (EDS) X-ray element mapping (Fig. 1*F*).

After the thread was made, the formation of an alginate hydrogel layer or the fabrication of a TRAFFIC device was achieved through a simple, one-step, in situ cross-linking process (Fig. 1*B*). In a typical process, a 2% (wt/vol) alginate solution [e.g., ultrapure sterile SLG100 alginate dissolved in a 0.9% (wt) NaCl solution] was placed in a tubular mold or a channel reservoir, and a modified thread was then inserted into the alginate solution. After a 4-min cross-linking, the entire device was taken out and placed in a Ca/Ba solution (typically 95 mM $CaCl_2$ and 5 mM $BaCl_2$) for 5 min for further cross-linking. The hydrogel layer that formed around the thread was uniform (Fig. 1 *G* and *H*), and the thickness could be controlled by adjusting the amount of incorporated $CaCl_2$ and the cross-linking time (see *SI Appendix*, SI-3 for details). In addition, examination of the interface between the nanoporous thread and the hydrogel in a lyophilized sample (Fig. 1*I*) seemed to suggest that the hydrogel infiltrated into the porous surface, which was believed to contribute to the strong thread–hydrogel adhesion. For cell encapsulation, the process was similar and an alginate solution containing cells or cell aggregates such as rat islets (Fig. 1*J*) was used for cross-linking. It is noted that the continuous nanoporous modification of the thread, resulted from the twisted helical structure and the evaporative cooling, and the internal release of Ca^{2+} are both of great significance to this encapsulation design. Simple sequential dipping of a conventional thread (i.e., bare suture) into a $CaCl_2$ solution and an alginate solution resulted in much less well-controlled hydrogel formation (*SI Appendix*, SI-4) (41). Our biomimetic thread may be used as an off-the-shelf, ready-to-use product for cell encapsulation conveniently at the research or transplantation place.

Characterizations of the Mechanical Robustness, Mass Transfer Property, and Biocompatibility

To show the mechanical robustness of the TRAFFIC device, we measured both the tensile strength of the whole device and the adhesion between the thread and the hydrogel. Compared with neat alginate hydrogel fiber, TRAFFIC exhibited drastically higher strength (Fig. 2*A*). More importantly, the hydrogel–thread adhesion in TRAFFIC was also remarkably high, much higher than the device made from the nonuniform beads-on-a-string thread or the one made by sequential dipping of a bare suture (Fig. 2*B* and *SI Appendix*, SI-5). We attributed the high adhesion to both the nanoporous surface structure (similar to the adhesion of water droplets to spider silks) and the macroscopic helices from the twisting of sutures (see *SI Appendix*, SI-5 for detailed analysis). To further demonstrate the necessity of the thread reinforcement for easy handling, we compared the TRAFFIC with a neat alginate fiber. As shown in Fig. 2*C*, the TRAFFIC was much more mechanically robust and easier to handle (also see Movies S1 and S2). In addition, the neat alginate fiber can clump or entangle with

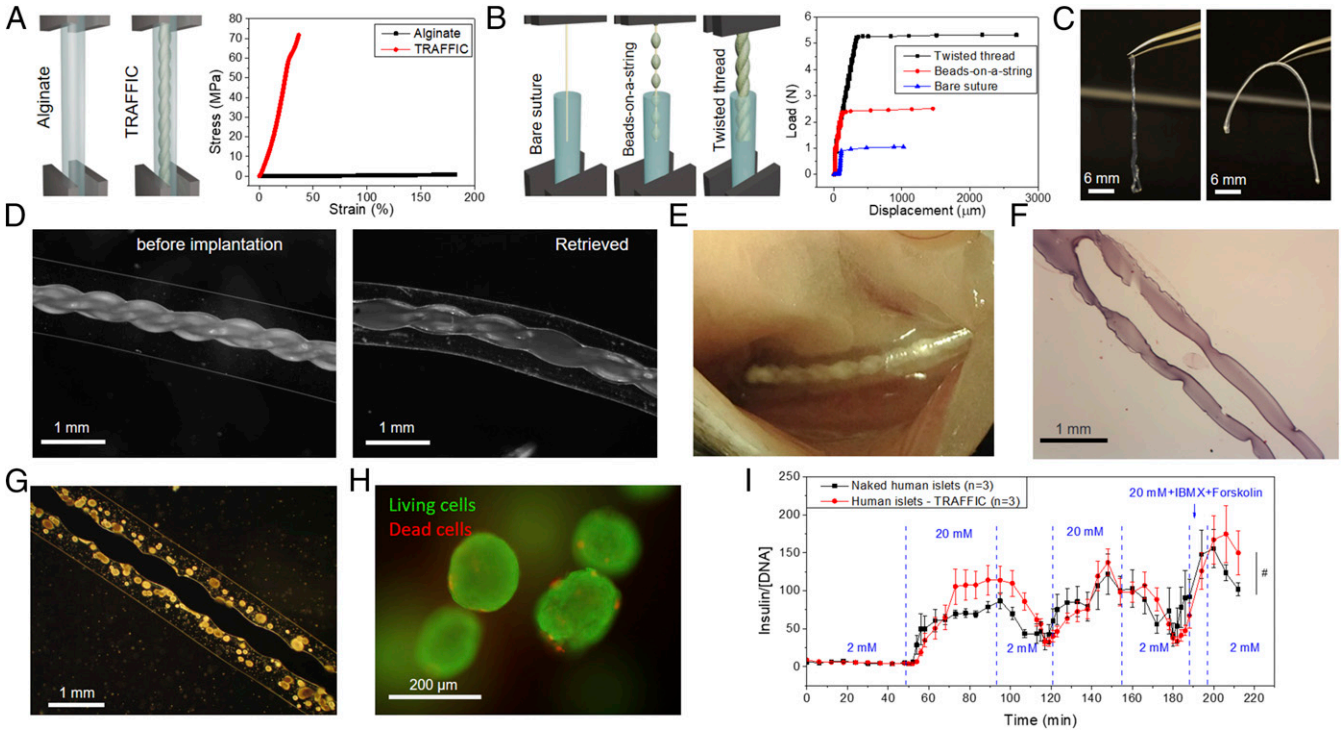

Fig. 2. Characterizations of the mechanical robustness, biocompatibility, and mass transfer property of TRAFFIC. (*A*–*C*) Mechanical robustness test: (*A*) strain-stress measurement, (*B*) load-displacement measurement, and (*C*) comparison between a neat alginate fiber and a TRAFFIC device in handling. (*D*–*F*) Biocompatibility characterization: (*D*) Microscopic images of TRAFFIC before implantation and after 7-mo implantation in mice. (Note that the devices shrank slightly after being transferred into a 4% paraformaldehyde for fixation.) (*E*) Digital photo of the device in the i.p. space of a mouse during the retrieval. (*F*) An H&E-stained image of a retrieved device ($n = 11$; see *SI Appendix*, SI-7 for complete data). (*G*–*I*) Mass transfer property: (*G*) microscopic image of the TRAFFIC device encapsulating human islets, (*H*) live (green)/dead (red) staining of encapsulated human islets, and (*I*) the glucose-stimulated human insulin secretion in a dynamic perifusion test, $n = 3$, mean ± SEM, $^{\#}P > 0.05$.

itself within the peritoneal cavity, jeopardizing the mass transfer or causing fibrosis (*SI Appendix*, SI-6). The mechanical robustness and easier handling are important advantages during implantation and retrieval.

Next, we investigated the biocompatibility of TRAFFIC. In cell encapsulation, the biocompatibility of the encapsulating material is one of the most important factors; foreign body reaction-induced fibrosis can negatively affect the mass transfer and the viability of encapsulated cells (42, 43). In recent years, much progress has been made on the biocompatibility of alginate materials, including both purity and formulation (25, 30). Particularly, it has been shown that increasing the size of intraperitoneally implanted alginate capsules from ∼500 μm to ∼1.5 mm reduced fibrosis (29). Inspired by these studies, we tested TRAFFIC with different thicknesses of the alginate layer in immunocompetent C57BL/6 mice and found that the thick device (overall diameter ∼ 1.3 mm) had less cellular overgrowth than the thinner ones (∼500 μm) after 2 wk of i.p. implantation (*SI Appendix*, SI-7). We believe this difference could be caused by many factors such as stiffness and surface area (*SI Appendix*, SI-7), and future work and more quantitative immunological studies are needed to elucidate the exact mechanisms. Nevertheless, encouraged by the short-term results, we further conducted longer term studies (3 mo, $n = 6$; 7 mo, $n = 11$). In the 3-mo study (*SI Appendix*, SI-7), while the thin devices induced variable cellular overgrowth, the thick ones had significantly less, consistent with the 2-wk results. Interestingly, even after 7 mo of implantation, 10 out of the 11 thick devices remained almost free of fibrosis (Fig. 2 *D–F* and *SI Appendix*, SI-7). In the following tests of function and demonstration of scalability and retrievability, the thick device design was used.

Another factor that is critical to the function of an encapsulation device is the mass transfer property (44). In the TRAFFIC design, since the cells are encapsulated in alginate hydrogel that has been proven to have facile mass transfer and since all of the cells are near the surface, we hypothesized that the mass transfer would be sufficient to support the cell survival and function. Indeed, experiments with human islets (Fig. 2 *G* and *H*) and several other types of cells (*SI Appendix*, Fig. S18) confirmed the cell viability in in vitro cultures. In addition, we performed a dynamic glucose-stimulated insulin secretion (GSIS) experiment using an islet perifusion system. The islets were subjected to Krebs–Ringer bicarbonate Hepes (KRBH) buffers with low (2 mM) or high (20 mM) glucose concentrations continuously in an alternating pattern, and the secreted insulin was measured. The results showed that both the nonencapsulated and encapsulated human islets could sense the glucose concentration change and secrete insulin (Fig. 2*I*). Application of 3-isobutylmethylxanthine (IBMX) and forskolin was included as a positive control and increased the insulin secretion in both cases. Although there appeared to be a delay in response for encapsulated islets, statistical analysis (see details in *Methods*) showed no significant difference in both total insulin secretion and the kinetics in this experiment. The facile mass transfer was probably due to the short diffusion distance (i.e., proximity of encapsulated islets to the surface). Previous studies have shown that the short diffusion distance was beneficial for not only cell survival but also glucose responsiveness (14, 45). We also measured the mass transfer of TRAFFIC more directly using different molecular weight, FITC-labeled dextran standards. The results indicated that the device would prevent the diffusion of molecules larger than ∼250 kDa (*SI Appendix*, SI-8).

Diabetes Correction in Mice

After confirming the mechanical robustness, biocompatibility, and mass transfer property of TRAFFIC, we explored its therapeutic potential. We transplanted encapsulated rat islets into the peritoneal cavity of streptozotocin (STZ)-induced C57BL/6 diabetic mice ($n = 10$ pooled from two independent experiments). This "rat-to-mouse" model has been used extensively in the field, and alginate hydrogel materials have been shown to be effective to protect xenografts without immunosuppression (27). Each diabetic mouse received a device of ∼1-inch length containing ∼475 ± 25 islet equivalents (IEQs) (Fig. 3*A*) (46). (Note that the cell survival posttransplantation was not studied, and therefore, the actual, functional IEQs inside a mouse was unknown.) The BG level of the mice decreased to the normal glycemic range (BG < 200 mg/dL) 2 d after the transplantation, and the mice remained cured for 4 wk before the devices were retrieved. After retrieval, the mice returned to a diabetic state, indicating the effectiveness of the device in regulating the BG (Fig. 3*B*). An i.p. glucose tolerance test (IPGTT) was conducted on day 28 after transplantation, before retrieval. The BG increased to more than 400 mg/dL in both healthy and diabetic mice after an i.p. injection of glucose solution (2 g of glucose per 1 kg of body mass). The BG of the transplanted mice gradually dropped to normal range within 120 min, further confirming the function of transplanted islets (Fig. 3*C*). The retrieved devices showed no tissue adhesion or significant fibrosis (Fig. 3*D*). An in vitro static GSIS (Fig. 3*E*) test of the retrieved devices suggested that the islets were responsive to glucose increase and secreted insulin, indicating the viability and normal function of the retrieved islets. Moreover, histological studies (Fig. 3*F*) showed minimal cellular overgrowth around the devices and normal morphology of islets with positive staining of insulin (Fig. 3*G*).

In another set of 1-mo transplantation experiments, we also included a control group of rat islets encapsulated in neat alginate fibers and a control group of BALB/c mouse islets encapsulated in TRAFFIC (Fig. 3*H* and *SI Appendix*, SI-9). With a similar number of rat islets (∼475 ± 25 IEQ), TRAFFIC performed similarly to the neat alginate fiber, confirming that the modified thread in TRAFFIC had no negative effect on the therapeutic potential. The results from rat islets and BALB/c mouse islets were also similar, although we used a lower IEQ (∼380 ± 20) for mouse islets. These control experiments confirmed the immunoprotective function of TRAFFIC for at least 1 mo, similar to neat alginate fibers. However, compared with the neat alginate fibers, TRAFFIC had much more robust mechanical properties that were critical for handling, retrieval, and scale-up. To examine whether TRAFFIC could have a longer term function, we conducted two independent 3-mo transplantation experiments using the rat-to-mouse model with a control group of unencapsulated rat islets transplanted in kidney capsules (in total, $n = 14$ for TRAFFIC and $n = 8$ for kidney capsules). For the mice with kidney capsule transplantation of unencapsulated islets, the BG level was decreased briefly after transplantation, suggesting that the primary graft function was achieved. However, the transplants were rapidly rejected, all within 2 wk. In contrast, TRAFFIC protected the islets from rejection and cured 10 out of 14 mice for at least 3 mo (Fig. 3*I* and *SI Appendix*, Fig. S21). The normal morphology of islets retrieved from cured mice as shown by the H&E staining and the positive immunohistochemical staining of insulin and glucagon confirmed the islet function in the device (Fig. 3*J*).

To further demonstrate the function of TRAFFIC, we performed more experiments in a different transplantation model using human islets. Given the large species difference between human and mouse, we chose immunodeficient SCID-Beige mice as recipients to minimize the complication of immune responses that occur in xenogeneic transplantation (47). We first tested the viability of encapsulated human islets (Fig. 4*A*) in nondiabetic SCID-Beige mice. The devices were retrieved after 1 mo and had minimal cell attachment and fibrosis (Fig. 4 *B* and *C*). Live/dead staining (Fig. 4*D*) and in vitro GSIS (Fig. 4*E*) of the retrieved islets indicated high viability and expected function. Next, we transplanted encapsulated human islets into STZ-induced diabetic SCID-Beige mice. We considered the mice to be diabetic when we had two consecutive measurements over 300 mg/dL, which we acknowledge was a relatively low standard for diabetes. However,

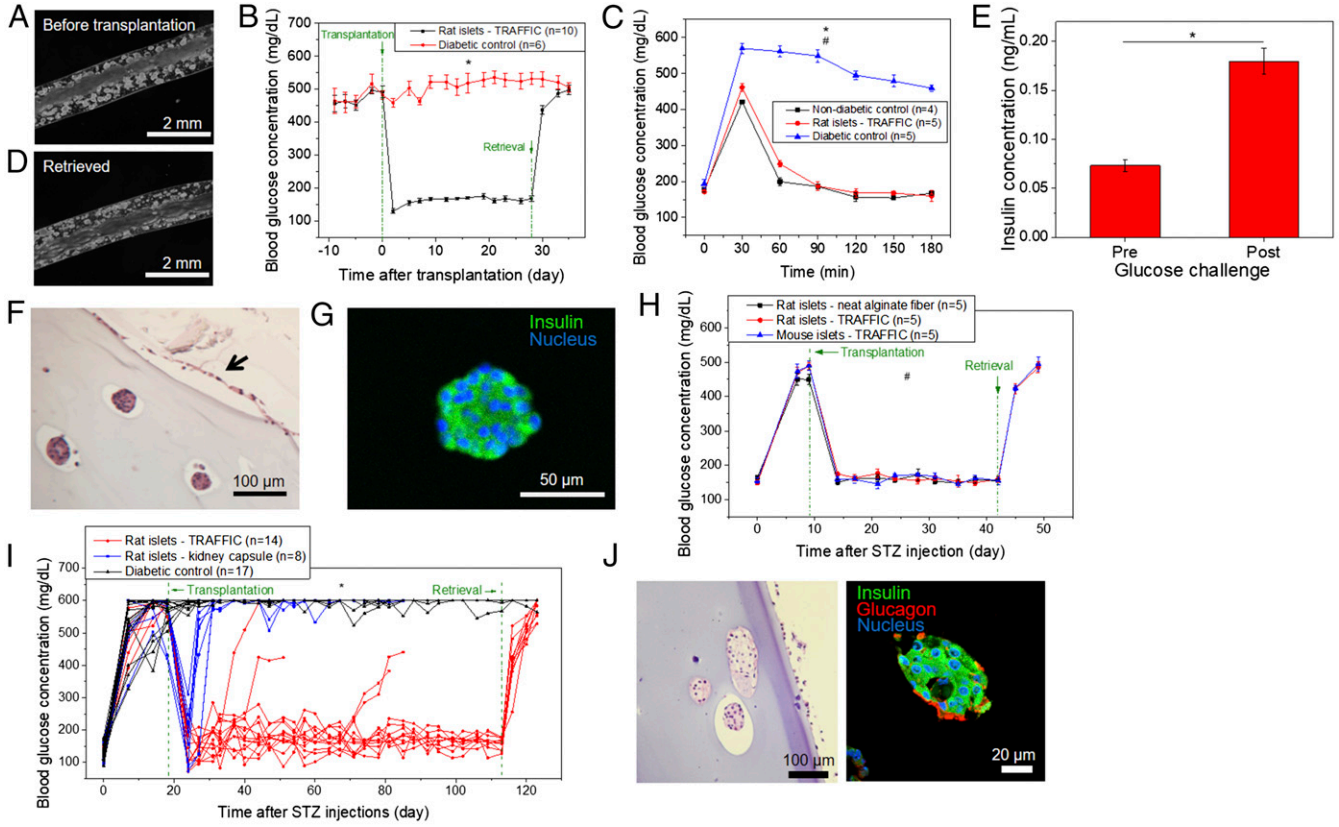

Fig. 3. Demonstration of therapeutic potential of TRAFFIC using rat islets. (*A*) Microscopic image of a TRAFFIC device encapsulating rat islets before transplantation. (*B*) BG concentration of diabetic C57BL/6 mice after transplantation of encapsulated rat islets, $n = 6–10$, mean ± SEM, $^{*}P < 0.05$. (*C*) IPGTT before retrieval on day 28, $n = 4–5$, mean ± SEM, $^{*}P < 0.05$ (diabetic control versus rat islets—TRAFFIC), $^{\#}P > 0.05$ (nondiabetic control versus rat islets—TRAFFIC). (*D*) A microscopic image of the retrieved device. (*E*) In vitro GSIS test of the retrieved rat islets, $n = 3$, mean ± SEM, $^{*}P < 0.05$. (*F*) H&E staining of cross-sections of retrieved islets (the arrow points to the cellular overgrowth on the device). (*G*) Immunohistochemical staining of the islets in a retrieved device (green, insulin; blue, nuclei). (*H*) BG concentrations of diabetic C57BL/6 mice after transplantation of rat islets encapsulated in neat alginate fiber or TRAFFIC and allogenic mouse islets encapsulated in TRAFFIC, $n = 5$, mean ± SEM, $^{\#}P > 0.05$ (among all three groups). (*I*) BG concentrations of mice from 3-mo transplantation studies, $n = 8–17$, mean ± SEM, $^{*}P < 0.05$ (diabetic control versus rat islets—TRAFFIC). (*J*) H&E staining and immunohistochemical staining of retrieved islets in TRAFFIC.

when we measured mouse c-peptide for the nontransplanted control groups, we found that the average was 42.7 pM for the STZ-treated group (94 d after STZ treatment) and 123.2 pM for the nontreated group. The c-peptide comparison in combination with the BG levels indicated that the mice had lost a substantial part of the beta cell mass due to the STZ treatment. Each STZ-treated mouse received two devices ∼1 inch long containing ∼1,900 ± 100 IEQs in total (48, 49). Nonencapsulated human islets of a similar number were transplanted in kidney capsules as a control. The BG and body weight were monitored over time. It took over 2 wk after transplantation to reverse the hyperglycemia. This slow response could be due to the species difference and/or the islet quality; similarly, slow BG reduction was observed previously following transplantation of human islets into kidney capsules of immunodeficent diabetic mice (49). However, after the initial diabetes correction, the BG levels of the mice in both the device and kidney capsule groups were maintained within the normal range for more than 4 mo until the experiment ended (Fig. 4*F*). In addition, the mice in both groups gained weight after transplantation, compared with the diabetic control group (Fig. 4*G*). Immunohistochemical staining showed positive staining of human insulin, Nkx-6.1, and glucagon in the islets retrieved from both kidney capsule and TRAFFIC, similar to the islets before transplantation (Fig. 4*H*). Assembled together, these data provide an important proof of concept for the use of TRAFFIC for T1D treatment.

Scale-Up and Test of Retrievability in Dogs

Two important advantages of the TRAFFIC design are scalability and retrievability. It is estimated that 500,000 IEQs may be needed to cure a human T1D patient (50). To deliver such a large number of islets, scalability is critical to any successful cell encapsulation system. Due to the thin cylindrical geometry, TRAFFIC can be scaled up in the longitudinal direction to a large capacity and can still be retrieved through minimally invasive laparoscopic procedures. To prove this concept, we fabricated ∼10-inch TRAFFIC devices using a custom-made thread holder and a channel reservoir (*SI Appendix*, Fig. S22 *A* and *B*). The device can be further scaled up by using a zigzag channel reservoir or tying multiple TRAFFIC devices together (see *SI Appendix*, SI-10 for details). Next, we performed some large animal experiments using dogs. In an initial pilot experiment, a ∼1.5 mm-diameter, 10 inch-long device (without cells) made from the beads-on-a-string thread (*SI Appendix*, Fig. S22*B*) was laparoscopically implanted into each of two dogs. The procedure was relatively simple and fast. Briefly, the device was placed in a pipette, which was then inserted through a laparoscopic trocar (*SI Appendix*, Fig. S22 *C* and *D* and *SI Appendix*, SI-11). Under the laparoscopic visualization, the device was pulled into the peritoneal cavity using laparoscopic forceps (*SI Appendix*, Fig. S22*C*, *Left*) and placed in the cranial abdomen near the liver. Two weeks later, the device was retrieved by grasping and pulling the device using a similar laparoscopic procedure (*SI Appendix*, Fig. S22*C*, *Right*). In one dog,

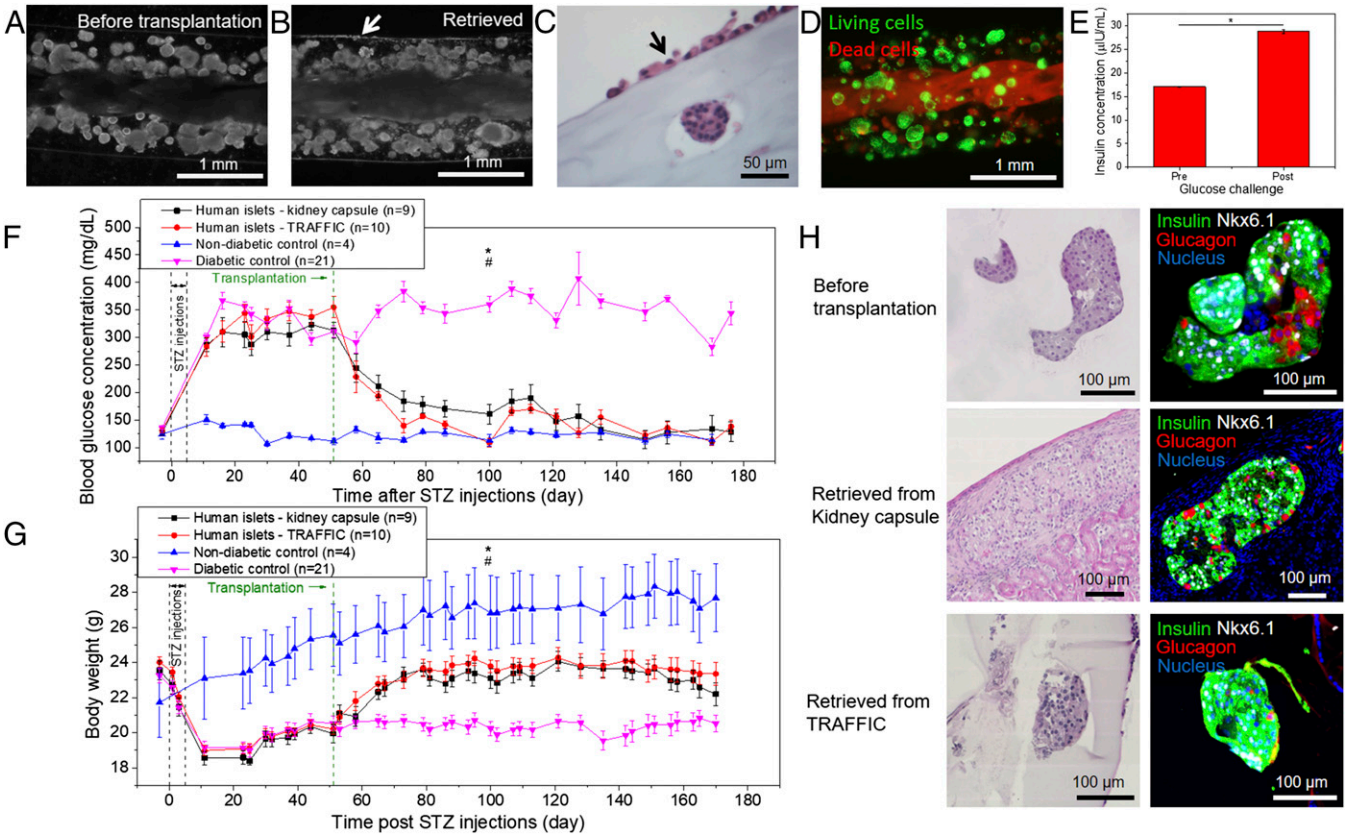

Fig. 4. Demonstration of the therapeutic potential of TRAFFIC using human islets. (*A*) Microscopic image of a TRAFFIC device with encapsulated human islets before transplantation. (*B*) Microscopic image of a TRAFFIC device retrieved after 1 mo. (*C*) H&E staining of a cross-section of the device (the arrow points to the minimal cellular overgrowth on the device). (*D*) Live (green)/dead (red) staining of human islets in retrieved device. (*E*) In vitro GSIS test of human islets in a retrieved device, $n = 3$, mean ± SEM, $^{*}P < 0.05$. (*F*) BG concentrations of diabetic SCID-Beige mice after transplantation of human islets, $n = 4$–21, mean ± SEM, $^{*}P < 0.05$ (human islets—TRAFFIC versus diabetic control), $^{\#}P > 0.05$ (human islets—kidney capsule versus human islets—TRAFFIC). (*G*) Body weights of the mice after transplantation. $n = 4$–21, mean ± SEM, $^{*}P < 0.05$ (human islets—TRAFFIC versus diabetic control), $^{\#}P > 0.05$ (human islets—kidney capsule versus human islets—TRAFFIC). (*H*) H&E staining and immunohistochemical staining of human islets before transplantation and retrieved from kidney capsules or TRAFFIC.

minor tissue adhesion occurred between the omentum and a segment of the device in which the hydrogel had detached and the thread was exposed (*SI Appendix*, Fig. S25). However, the device was still retrievable in its entirety after excising the adhered tissue. In the other dog, there was no adhesion or any gross fibrosis on the device (*SI Appendix*, Fig. S22 *E* and *F*). Remarkably, even though the device left an indentation on the liver (*SI Appendix*, Fig. S22*E*), there was no fibrosis or histologic indication of inflammation in the tissue (*SI Appendix*, Fig. S22*G*). In both dogs, there were no significant changes in bloodwork (i.e., fibrinogen concentration, white blood cell count, liver enzyme concentrations), suggesting that no inflammation was induced.

Although this first pilot experiment was promising, comparison of the results from the two dogs highlighted the importance of the thread design to ensure strong hydrogel–thread adhesion. To overcome the hydrogel detaching problem that occurred in one of the dogs, we repeated the implantation experiment with three more dogs using a device (diameter of ∼2 mm) made from the continuously modified, twist-folded thread. One dog was implanted with an empty device while the other two were implanted with devices encapsulating subtherapeutic doses of rat islets (∼1,000 IEQs per device). The devices were retrieved after 1 mo. All three devices remained intact, and no tissue adhesion occurred (*SI Appendix*, Fig. S26 and Movie S3). To illustrate the convenient retrieval, we took videos both inside and outside the dog (Fig. 5 *A* and *B*). The retrieval was simple and rapid; it took merely 10 s from grasping the device to removal (Movies S4 and S5). The retrieved devices had only thin layers of attached cells (Fig. 5 *C* and *D*). The xenogeneic rat islets induced some local inflammation (*SI Appendix*, Fig. S26), however there was no tissue adhesion and the devices were still easily retrievable. More importantly, the islets in retrieved devices were still viable and functional, as evidenced by live/dead staining (Fig. 5*E*), insulin staining of cross-sectioned islets (Fig. 5*F*), and in vitro GSIS (Fig. 5*G*).

Discussion

Recent development of stem cell biology has brought tremendous hope that one day human stem cells may be differentiated into functional beta-like cells and transplanted into T1D patients (11, 51, 52). However, to prevent immune and autoimmune attack, the exogenous cells need to be encapsulated or immunoprotected. Developing an encapsulation system that can be clinically used has unfortunately been a great challenge (5, 7, 11, 12). Planar diffusion chambers such as the Viacyte device have shown great promise in preclinical small animal studies (53). However, there are considerable challenges to scale up the device to human patients due to the intrinsically low surface area for mass transfer; high cell packing density may lead to deficiency of oxygen and nutrients (7, 13, 14). The other major type of encapsulation system is the hydrogel capsule. Hydrogel capsules have a larger surface area and can potentially deliver a higher number of islets (5, 7, 29, 54). Importantly much progress has been made recently on the biocompatibility of

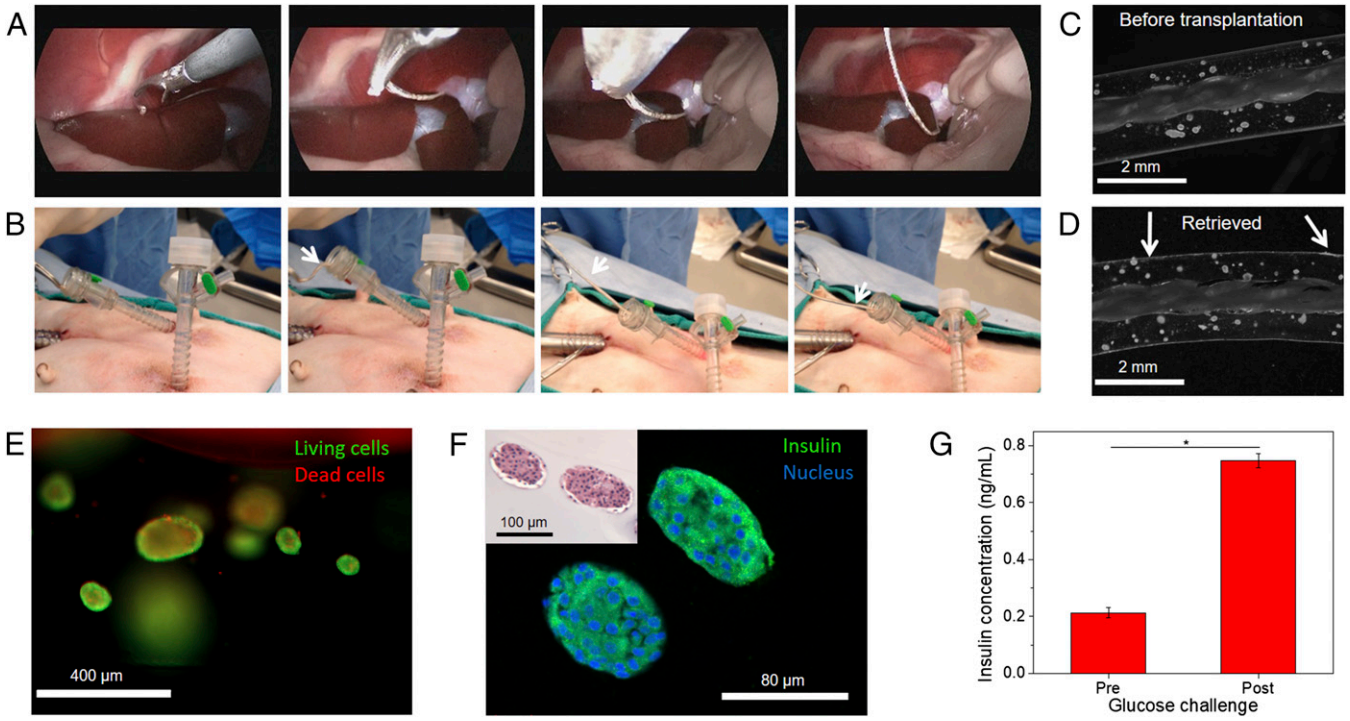

Fig. 5. Demonstration of rapid device retrieval and cell survival in a dog model. (*A*) A series of laparoscopic images showing the retrieval process. (*B*) A series of digital images showing the device being pulled out from a trocar. (*C* and *D*) Microscopic images of the device with encapsulated rat islets before (*C*) and after (*D*) transplantation in dogs (the arrow points to the minimal cellular overgrowth on the device). (*E*) Live/dead staining of retrieved rat islets. (*F*) Insulin staining of retrieved islets. (*Inset*) H&E staining. (*G*) In vitro GSIS, $n = 3$, mean ± SEM, $^*P < 0.05$.

alginate hydrogels (30, 43), which makes the capsules more functionally durable and easier to retrieve. However, common retrieval techniques such as aspiration and lavage are time-consuming, and it is a great challenge to ensure complete retrieval given the large capsule number and the complicated organ structures inside the peritoneal space (8, 18, 32). Incomplete retrieval can cause serious safety concerns when stem cell-derived cells are used due to the potential of teratoma formation (5, 55).

In this work, we report an encapsulation design that takes advantages of alginate hydrogel and is both scalable and retrievable. The key to the design is a tough central thread with continuous nanoporous modification and uniform Ca^{2+} release. The device is in contrast to conventional neat hydrogel fibers, which although previously proposed for cell encapsulation (56–61) were soft and easy to break and therefore not suited for clinical applications. The uniform and controllable hydrogel thickness as well as the strong thread–hydrogel adhesion are important for both function and translation. Convenient retrieval with a minimally invasive surgery would be particularly attractive for clinical applications. For any transplantation, straightforward removal after completion of therapy or failure of transplant would address patients' concerns of having foreign materials and cells permanently implanted in the body (5, 12, 33). As therapeutic cells derived from stem cells or adult cells become a potential alternative to primary cells, retrievability is more highly desired to mitigate the concerns of teratoma formation (5, 55). We believe this encapsulation design will minimize the risks and discomfort associated with transplantation, make repeated transplantation a more acceptable option, and therefore likely accelerate and contribute to the translation of cell encapsulation for T1D and potentially many other diseases. Furthermore, our modified thread device could be available to researchers or clinicians as an off-the-shelf, ready-to-use product, and cell encapsulation may be performed at site via a one-step in situ cross-linking.

Methods

Chemicals. Calcium chloride ($CaCl_2$), barium chloride ($BaCl_2$), sodium chloride (NaCl), PMMA, DMF, glucose stock solution, human serum albumin, and IBMX were purchased from Sigma-Aldrich Co. Forskolin was purchased from Tocris Bioscience. Glutamax was purchased from Life Technologies. KRBH was purchased from VWR. Glucose was purchased from Mallinckrodt Pharmaceuticals. Ultrapure, sterile sodium alginate (SLG100) was purchased from FMC BioPolymer Co. [Note that alginates used in this study had no significant amount of endotoxin according to a previous publication (30).] Water was deionized to 18.2 MΩ-cm with a Millipore purification system.

Animals. C57BL/6 and BALB/c mice were purchased from The Jackson Laboratory. SCID-Beige mice for transplantation experiments were obtained from Taconic Farms. Sprague–Dawley rats for isolation of pancreatic islet cells were obtained from Charles River Laboratories. Beagle dogs for implantation were obtained from Marshall Bioresources. All animal procedures were approved by the Cornell Institutional Animal Care and Use Committee. Transplantation of encapsulated human islets in diabetic SCID-Beige mice was performed at Novo Nordisk A/S, and the protocols were approved by the Danish Animal Experimentation Inspectorate and carried out by trained and licensed personnel.

Characterizations. The samples were characterized by different analytical techniques. Scanning electron microscopy (SEM) and EDS element mapping were performed by using a field emission scanning electron microanalyzer (LEO 1550). Optical and fluorescent microscopic images were observed using a digital inverted microscope (EVOS fl). Conventional macrotensile measurements were performed using a dynamic mechanical analysis (DMA Q800). All samples were mounted between holders at a distance of ~1.5 cm. Tensile testing was conducted at a rate of 0.5 N/min at room temperature (23 °C). Stress (MPa) and strain (%) were automatically calculated by the software. Confocal images were taken by using a Laser Scanning Confocal Microscope (LSM 710).

Fabrication of Modified Threads. Typically, two sterile sutures (Ethilon nylon suture, 5–0, monofilament, Ethicon, Inc.; KRUUSE nylon suture, 5–0, Jørgen Kruuse A/S) were twisted together to accumulate some torsion. Then, the twisted sutures were folded in the middle, which causes the sutures to self-twist again to release the torsion. Knots were made at the end of the

twisted sutures to prevent the sutures from untwisting. Then, the sutures were submerged into 7% (wt/vol) PMMA/DMF solution, containing 2.5% (wt/vol) $CaCl_2$, for ~3 s. The sutures were taken out from the polymer solution and air dried. After the modification was finished, all of the sutures were sterilized by ethylene oxide or by autoclave in dry mode before use.

Rat Islet Isolation and Purification. Sprague–Dawley rats from Charles River Laboratories weighing ~300 g were used for harvesting islets. All rats were anesthetized using 3% isoflurane in oxygen and maintained at the same rate throughout the procedure. Isolation surgeries were performed as described by Lacy and Kostianovsky (62). Briefly, the bile duct was cannulated, and the pancreas was distended by an in vivo injection of 0.15% Liberase (Research Grade, Roche) in RPMI 1640 media solution. The pancreas was digested in a 37 °C water bath for 30 min. The digestion was stopped by adding 10–15 mL of cold M199 media with 10% heat-inactivated FBS and a slight shaking. Digested pancreases were washed twice in the same aforementioned M199 media, filtered through a 450 μm sieve, and then suspended in a Histopaque 1077 (Sigma)/M199 media gradient and centrifuged at 1,700 × *g* at 4 °C. This gradient centrifugation step was repeated for higher purity islets. Finally, the islets were collected from the gradient and further isolated by a series of gravity sedimentations, in which each supernatant was discarded after 4 min of settling. Purified islets were hand-counted by aliquot under a light microscope and then washed three times in sterile PBS. Islets were then washed once in RPMI 1640 media with 10% heat-inactivated FBS and 1% penicillin/streptomycin and cultured in this medium overnight for further use.

Cell Encapsulation. For a typical mouse device, the modified thread was inserted into a polyethylene tube (~1.5 mm inner diameter). A predetermined amount of cell-loaded alginate solution [e.g., ~500 IEQs dispersed in ~60 μL 2% (wt/vol) alginate solution] was filled into the tube using a micropipette and left for 4 min. Then, the TRAFFIC device was carefully pulled out of the tube using tweezers. Most alginate and cells were incorporated into the device, and the leftover alginate in the tube was usually unnoticeable with a small number of islets adhered to the tube wall. It was estimated from multiple observations that the encapsulation efficiency was at least 90% (data analyzed and estimated from five isolations with ~30 independent trials). Given the ~500 IEQs with which we started, we determined the actual IEQ for transplantation was 475 ± 25. The device was further cross-linked by a cross-linking buffer containing 95 mM $CaCl_2$ and 5 mM $BaCl_2$. Next, the device was washed three times with 0.9% (wt/vol) saline and transferred into corresponding cell culture medium. Islets were typically treated as following for encapsulation. Immediately before encapsulation, the cultured islets were centrifuged at 392 × *g* for 1 min and washed with Ca-free Krebs–Henseleit (KH) buffer (4.7 mM KCl, 25 mM Hepes, 1.2 mM KH_2PO_4, 1.2 mM $MgSO_4.7H_2O$, 135 mM NaCl, pH ~ 7.4, osmotic pressure ~ 290 mOsm). After the wash, the islets were centrifuged again, and all supernatants were aspirated. Then, the collected islets were encapsulated following the procedure described above. The TRAFFIC devices encapsulating cells were checked under microscope to ensure that no cells were exposed on the hydrogel surface. Since the islets had variable sizes (50–400 μm), the total number of encapsulated islets were converted into islet equivalences (IEQs, normalized to 150 μm size) based on a previously published method (46).

Static GSIS Assay. Krebs Ringer Bicarbonate (KRB) buffer [2.6 mM $CaCl_2{\cdot}2H_2O$, 1.2 mM $MgSO_4.7H_2O$, 1.2 mM KH_2PO_4, 4.9 mM KCl, 98.5 mM NaCl, and 25.9 mM $NaHCO_3$ (all from Sigma-Aldrich) supplemented with 20 mM Hepes/Na-Hepes (Roche) and 0.1% BSA (Serological)] was prepared beforehand. Encapsulated islets were incubated for 2 h in KRB buffer at 37 °C, 5% CO_2, and then incubated for 75 min with 2.8 mM or 16.7 mM glucose under the same condition. Insulin concentrations in the buffer solutions were determined by using ultrasensitive mouse/rat insulin ELISA kit (Crystal Chem) or human insulin ELISA kit (ALPCO) per suppliers' protocols. For devices retrieved from mice, three out of five retrieved TRAFFIC devices were tested with the GSIS assay (the remaining two devices were fixed right after retrieval and submitted for histology); for devices retrieved from dogs, three independent regions of the retrieved devices were cut and tested with the GSIS assay. All of the ELISA results were normalized to the IEQs.

Perifusion Test. Human islets were purchased from Prodolabs. Upon receipt, viability was assessed with the LIFE/DEAD Viability/Cytotoxicity kit (calcein-AM staining indicating living cells and ethidium homodimer-1 staining indicating dead cells) according to the manufacturer's instructions (Invitrogen). Dynamic insulin release was examined with a perifusion system from Biorep according to the manufacturer's guidelines. In short, 250 hand-picked human islets or 1/3 device (expected 500 IEQ) were loaded on columns surrounded by Bio-Gel P-4 beads (Biorad) and allowed to acclimate for 60 min in KRBH containing 2 mM glucose at 100 μL/min flow (kept constant during the experiment). Islets were then exposed to different glucose concentrations and/or factors, and secreted insulin was collected in defined time frames. After the experiment, islets were collected and lysed [tissue extraction reagent I (Invitrogen) + tissue lyzer (Qiagen)]. The insulin concentration was measured and normalized to DNA concentration (PicoGreen dsDNA kit; Thermofisher).

Implantation and Retrieval in Mice. Immune-competent male C57BL/6 mice and immunodeficient SCID-Beige mice were utilized for transplantation. To create insulin-dependent diabetic mice, healthy mice were treated (50 mg/kg mouse) with freshly prepared STZ (Sigma-Aldrich) solution (7.5 mg/mL in sodium citrate buffer solution) for 5 consecutive days. The BG levels of all mice were retested before transplantation. Only mice whose nonfasted BG levels were above 300 mg/dL for two consecutive measurements were considered diabetic and underwent transplantation. The nondiabetic or STZ-induced diabetic mice were anesthetized with 3% isoflurane in oxygen, and their abdomens were shaved and sterilized using betadine and 70% ethanol. Preoperatively, all mice received 0.3 mL of 0.9% saline s.c. to prevent dehydration. A ~1-mm incision was made along the midline of the abdomen, and the peritoneal lining was exposed using blunt dissection. The peritoneal wall was then grasped with forceps, and a ~1-mm incision was made along the linea alba. The device was then inserted into the peritoneal cavity through the incision. The incision was closed using 5–0 taper polydioxanone (PDS II) absorbable sutures. The skin was then closed over the incision using a wound clip. The devices were retrieved from mice at desired time points postimplantation or -transplantation (with encapsulated cells) using similar procedures except that larger (~5 mm) incisions were made in the skin and the peritoneum. The device was located, grasped, and pulled out by using blunt tweezers. After retrieval, the TRAFFIC devices were first submerged into a cross-linking solution containing 95 mM $CaCl_2$ and 5 mM $BaCl_2$ for ~5 min and then transferred into 4% paraformaldehyde for fixation or a cell culture medium for postcharacterization.

For the SCID-Beige mice and human islet study, the mice were rendered diabetic by five consecutive doses of STZ (70 mg/kg). During the first week after the STZ treatment, the mice were not intervened. After the first week, if the body weight of a mouse dropped more than 10%, the mouse was treated with insulin (NPH 100 nmol/kg 1× daily). The insulin treatment was independent of whether the mouse was from the experimental or control groups. Normally, the diabetic mice were used 3–4 wk after STZ treatment, but for this batch of experiments, mice were used about 45 d after treatment due to the logistics associated with human islet isolation and delivery. The TRAFFIC device transplantations were performed as described above, but anesthesia and analgesia procedures were performed as for the kidney capsule transplantation.

For the kidney capsule transplantation, mice were anesthetized using 5% isoflurane with O_2 flow set at 1 L for anesthetic induction (approx. 1–2 min). The anesthesia was maintained using 1–1.5% isoflurane. Rimadyl, 5 mg/kg s.c., was administered 30 min presurgery and 24 and 48 h postsurgery. Temgesic, 0.05 mg/kg, was dosed s.c. 30 min presurgery and 3–6 h postsurgery.

The sedated mice were shaved in the surgical area, more specifically the left lateral side of the mouse ~3 × 3 cm and about 2 cm from the last rib down. The skin was washed with iodide and ethanol. The shaved area was covered with barrier drape. A small incision through the skin and muscle of the left flank of the animal was made, and the kidney was exposed outside the body using two saline-moistened cotton-tipped applicators. The kidney capsule was sliced using a small needle leaving a small hole. A pouch was made using a rounded glass capillary, and a transfer pipette was used to transplant clusters of islets into the pouch. The kidney was returned to the peritoneal cavity, and the muscle layer was closed with a 4–0 absorbable suture and the skin closed with two to three staples.

Laparoscopic Implantation and Retrieval in Dogs. Dogs were premedicated with gylcopyrolate and butorphanol, induced with propofol, and anesthetized with isoflurane and oxygen. The abdomen was clipped and prepared for sterile surgery. A 10-mm laparoscopic camera port and two 5-mm instrument ports were percutaneously inserted into the abdomen. The abdomen was insufflated to 12 mm Hg pressure with CO_2. The device was inserted into the abdomen through the left-side instrument port. A laparoscopic probe was introduced through the right-sided 5-mm port and was used to manipulate the device so that it was placed between the liver and the diaphragm. The remaining ports were then removed, and the port sites were closed with 3–0 polydioxinone suture material. For retrieval of the devices, the procedure was similar using one 10-mm camera port and one or two 5-mm instrument ports. The previously implanted device was located and photographed. The device was grasped with laparoscopic Kelly forceps

inserted through a 5-mm port and dissected from the attached omentum if necessary using laparoscopic scissors. The device was then removed from the abdomen through the 5-mm port. The remaining laparoscopic ports were removed, and the dogs were humanely euthanatized.

BG Monitoring. BG levels were monitored three times a week in mice following transplant surgery. A small drop of blood was collected from the tail vein using a lancet and tested using a commercial glucometer (Clarity One, Clarity Diagnostic Test Group). Mice with unfasted BG levels below 200 mg/dL were considered normoglycemic. For the BG test in SCID-Beige mice, blood samples were obtained from the tip of the tail by puncturing the tail capillaries with a lancet in conscious mice. The blood (5 μL) was collected into Na-heparinized capillary tubes and transferred to 250 μL eBioscience haemolysing buffer. The glucose concentration was measured on Biosen 5040 S line glucose analyzer (Eppendorf).

Histological Analysis and Immunostaining. The retrieved devices were fixed in 4% paraformaldehyde, embedded in paraffin, and sectioned by Cornell Histology Core Facility. Paraffin sections 10 mm thick were stained with hematoxylin/eosin. For staining of insulin with immunofluorescence, paraffin-embedded sections were rehydrated by sequential washing in xylene; 100%, 95%, and 75% ethanol; and water. Then slides were boiled in 1 mM EDTA for antigen exposure. After blocking, primary guinea pig anti-rat insulin antibody (Linco,1:200) was applied and incubated overnight at 4 °C, followed by a wash and incubation with FITC-conjugated donkey anti-guinea pig IgG (Jackson Immunoresearch, 1:200). Slides were washed twice with water, applied with antifade/DAPI, and covered with coverslips. Fluorescence images were captured under a ZeissLSM710 confocal microscope. The histologic analysis of human islets is as follows: Devices and grafted kidneys were fixed in 10% natural buffered formalin, processed to paraffin, and sectioned (3 μm). Islet morphology was visualized with hematoxylin and eosin staining. Alpha and beta cells were visualized in a triple immunohistocemical stain with guinea pig anti-insulin (1/75 in 0.05% TNB; A0564; DAKO), rabbit anti-Nkx6.1 (1/1,000 in 0.05% TNB; HPA036774; Sigma-Aldrich), and mouse anti-glucagon (1/7800 in 0.05% TNB; Glu-001; Novo Nordisk). Insulin was visualized with goat–anti-guinea pig-488 (A11073; Invitrogen) and donkey–anti-goat-488 (705-545-147; Jackson). Nkx6.1 was visualized with donkey anti-rabbit-biotin (711-065-152; Jackson) and TSA cy3 (NEL704A001KT; Perkin-Elmer). Glucagon was visualized with donkey anti-mouse-Cy5 (715-175-151; Jackson). Antigens were first retrieved with TEG buffer (AMPQ17020; Ampliqon), after which slides were blocked with 1% hydrogen peroxide, avidin, biotin, and TNB buffer (0.05%). The slides were then incubated with primary antibodies for 45 min, secondary antibody and DAPI for 30 min, Streptavidin-PO (1:500) and tertiary antibody for 30 min, and TSA-cy3 substrate for 15 min, and finally the slides were mounted with a fluorescent mount (DAKO). The stains were visualized on an Olympus VS120 slide scanner.

Statistical Analysis. Results are expressed as mean ± SEM. The data were analyzed via Student's *t* tests and analysis of covariance (ANCOVA) followed by a Tukey post hoc test where appropriate. Treatment (i.e., TRAFFIC vs. diabetic control, vs. nondiabetic control, etc.) was considered as a factor, while time was treated as a continuous covariate. In many experiments, there were data collected before the treatment was applied and/or after the treatment was removed (e.g., before implantation of TRAFFIC and after retrieval). In these cases, only the data collected during the treatment period were analyzed. For Fig. 2*I*, rather than treating time as a continuous covariate, the area under the curve (AUC) was calculated for each time period during which the cells were exposed to a specific glucose concentration (i.e., either 2 mM or 20 mM glucose). Time period (from 1 through 5) was treated as an additional factor; thus, the ANOVA model consisted of AUC as the response variable with treatment (TRAFFIC vs. islets) completely crossed with time period in a full factorial design. ANCOVA assumes that the relationship between the response variable and each covariate is linear. While this is a good assumption for the majority of the data presented in this paper, in Fig. 3*C*, the initial spike in BG during the first 30 min of the experiment introduces some nonlinearity. To account for this, we analyzed the data from this figure twice; first, we included all data, and then we analyzed only the BG measurements taken after the first 30 min (when the response varied linearly with time). The statistical significance of the treatments did not change regardless of whether the first 30 min of data were included in the analysis. Therefore, the *P* values presented are from the analysis of all data, including the first 30 min. The sample sizes for the data presented in Fig. 4 *F* and *G* are not balanced. To ensure that this imbalance did not affect the validity of our analysis we followed a resampling procedure (63), taking a random sample of four animals (the size of the smallest treatment group) from each treatment group and recalculating both the ANCOVA and the Tukey post hoc test for each sample. This process was repeated 1,000 times. The reported *P* values are the median values from these 1,000 trials. It should be noted that while the *P* values from the resampling procedure are not identical to the *P* values obtained without the resampling procedure, the conclusions regarding statistical significance did not change.

ACKNOWLEDGMENTS. The authors thank Marianne Vollmond, Dorte Lauritsen, Hanne Nord Søndergaard, and Helene Dyhr for their excellent technical assistance. This work was partially supported by the American Diabetes Association (Grant 7-13-JF-42), the 3M Company, Novo Nordisk A/S, the Cornell Technology Acceleration and Maturation (CTAM) Fund, the Cornell Stem Cell Program Seed Fund, and the Hartwell Foundation. The work took use of the Cornell Center for Materials Research shared facilities, which are supported through the NSF Materials Research Science and Engineering Centers (MRSEC) program (Grant NSF DMR-1120296).

1. Wen L, et al. (2008) Innate immunity and intestinal microbiota in the development of type 1 diabetes. *Nature* 455:1109–1113.
2. Nathan DM, et al.; Diabetes Control and Complications Trial Research Group (1993) The effect of intensive treatment of diabetes on the development and progression of long-term complications in insulin-dependent diabetes mellitus. *N Engl J Med* 329: 977–986.
3. Shapiro AMJ, et al. (2006) International trial of the Edmonton protocol for islet transplantation. *N Engl J Med* 355:1318–1330.
4. Weir GC, Bonner-Weir S (1997) Scientific and political impediments to successful islet transplantation. *Diabetes* 46:1247–1256.
5. Desai T, Shea LD (2017) Advances in islet encapsulation technologies. *Nat Rev Drug Discov* 16:338–350.
6. Orive G, et al. (2003) Cell encapsulation: Promise and progress. *Nat Med* 9:104–107.
7. Dolgin E (2014) Encapsulate this. *Nat Med* 20:9–11.
8. Scharp DW, Marchetti P (2014) Encapsulated islets for diabetes therapy: History, current progress, and critical issues requiring solution. *Adv Drug Deliv Rev* 67-68: 35–73.
9. Calafiore R, Basta G (2014) Clinical application of microencapsulated islets: Actual prospectives on progress and challenges. *Adv Drug Deliv Rev* 67–68:84–92.
10. Vaithilingam V, Tuch BE (2011) Islet transplantation and encapsulation: An update on recent developments. *Rev Diabet Stud* 8:51–67.
11. Dolgin E (2016) Diabetes: Encapsulating the problem. *Nature* 540:S60–S62.
12. Orive G, et al. (2015) Cell encapsulation: Technical and clinical advances. *Trends Pharmacol Sci* 36:537–546.
13. Ledford H (2014) Stem-cell success poses immunity challenge for diabetes. *Nature* 514: 281.
14. Colton CK (2014) Oxygen supply to encapsulated therapeutic cells. *Adv Drug Deliv Rev* 67–68:93–110.
15. Papas KK, Avgoustiniatos ES, Suszynski TM (2016) Effect of oxygen supply on the size of implantable islet-containing encapsulation devices. *Panminerva Med* 58:72–77.
16. Papas KK, et al. (2013) Macroencapsulated human islet viability is drastically reduced in vivo as the number of islets per device is increased. *Transplantation* 96:S71.
17. Smink AM, Faas MM, de Vos P (2013) Toward engineering a novel transplantation site for human pancreatic islets. *Diabetes* 62:1357–1364.
18. Jacobs-Tulleneers-Thevissen D, et al.; Beta Cell Therapy Consortium EU-FP7 (2013) Sustained function of alginate-encapsulated human islet cell implants in the peritoneal cavity of mice leading to a pilot study in a type 1 diabetic patient. *Diabetologia* 56:1605–1614.
19. Wang T, et al. (1997) An encapsulation system for the immunoisolation of pancreatic islets. *Nat Biotechnol* 15:358–362.
20. Cui H, et al. (2009) Long-term metabolic control of autoimmune diabetes in spontaneously diabetic nonobese diabetic mice by nonvascularized microencapsulated adult porcine islets. *Transplantation* 88:160–169.
21. Soon-Shiong P, et al. (1993) Long-term reversal of diabetes by the injection of immunoprotected islets. *Proc Natl Acad Sci USA* 90:5843–5847.
22. Wang T, et al. (2008) Successful allotransplantation of encapsulated islets in pancreatectomized canines for diabetic management without the use of immunosuppression. *Transplantation* 85:331–337.
23. Elliott RB, et al. (2005) Intraperitoneal alginate-encapsulated neonatal porcine islets in a placebo-controlled study with 16 diabetic cynomolgus primates. *Transplant Proc* 37:3505–3508.
24. Sun Y, Ma X, Zhou D, Vacek I, Sun AM (1996) Normalization of diabetes in spontaneously diabetic cynomologus monkeys by xenografts of microencapsulated porcine islets without immunosuppression. *J Clin Invest* 98:1417–1422.
25. de Vos P (2014) Cell encapsulation: Ready for the next step. *Adv Drug Deliv Rev* 67–68: 1–2.
26. Elliott RB, et al. (2007) Live encapsulated porcine islets from a type 1 diabetic patient 9.5 yr after xenotransplantation. *Xenotransplantation* 14:157–161.
27. Omer A, et al. (2003) Survival and maturation of microencapsulated porcine neonatal pancreatic cell clusters transplanted into immunocompetent diabetic mice. *Diabetes* 52:69–75.

28. Orive G, Emerich D, De Vos P (2014) Encapsulate this: The do's and don'ts. *Nat Med* 20: 233.
29. Veiseh O, et al. (2015) Size- and shape-dependent foreign body immune response to materials implanted in rodents and non-human primates. *Nat Mater* 14:643–651.
30. Vegas AJ, et al. (2016) Combinatorial hydrogel library enables identification of materials that mitigate the foreign body response in primates. *Nat Biotechnol* 34: 345–352.
31. Vegas AJ, et al. (2016) Long-term glycemic control using polymer-encapsulated human stem cell-derived beta cells in immune-competent mice. *Nat Med* 22:306–311.
32. Tuch BE, et al. (2009) Safety and viability of microencapsulated human islets transplanted into diabetic humans. *Diabetes Care* 32:1887–1889.
33. Pepper AR, et al. (2015) A prevascularized subcutaneous device-less site for islet and cellular transplantation. *Nat Biotechnol* 33:518–523.
34. Matsumoto S, Tomiya M, Sawamoto O (2016) Current status and future of clinical islet xenotransplantation. *J Diabetes* 8:483–493.
35. Lindvall O, Wahlberg LU (2008) Encapsulated cell biodelivery of GDNF: A novel clinical strategy for neuroprotection and neuroregeneration in Parkinson's disease? *Exp Neurol* 209:82–88.
36. Zheng Y, et al. (2010) Directional water collection on wetted spider silk. *Nature* 463: 640–643.
37. Srinivasarao M, Collings D, Philips A, Patel S (2001) Three-dimensionally ordered array of air bubbles in a polymer film. *Science* 292:79–83.
38. Bognitzki M, et al. (2001) Nanostructured fibers via electrospinning. *Adv Mater* 13: 70–72.
39. Quéré D, di Meglio JM, Brochard-Wyart F (1990) Spreading of liquids on highly curved surfaces. *Science* 249:1256–1260.
40. Duprat C, Protière S, Beebe AY, Stone HA (2012) Wetting of flexible fibre arrays. *Nature* 482:510–513.
41. Akbari M, et al. (2014) Composite living fibers for creating tissue constructs using textile techniques. *Adv Funct Mater* 24:4060–4067.
42. Krishnan R, Alexander M, Robles L, Foster CE, 3rd, Lakey JR (2014) Islet and stem cell encapsulation for clinical transplantation. *Rev Diabet Stud* 11:84–101.
43. Bray N (2016) Biomaterials: Modified alginates provide a long-term disguise against the foreign body response. *Nat Rev Drug Discov* 15:158.
44. Gurruchaga H, et al. (2015) Advances in cell encapsulation technology and its application in drug delivery. *Expert Opin Drug Deliv* 12:1251–1267.
45. De Vos P, Wolters GHJ, Fritschy WM, Van Schilfgaarde R (1993) Obstacles in the application of microencapsulation in islet transplantation. *Int J Artif Organs* 16:205–212.
46. Ricordi C, et al. (1990) Islet isolation assessment in man and large animals. *Acta Diabetol Lat* 27:185–195.
47. Bruin JE, et al. (2015) Treating diet-induced diabetes and obesity with human embryonic stem cell-derived pancreatic progenitor cells and antidiabetic drugs. *Stem Cell Reports* 4:605–620.
48. Gaber AO, et al. (2004) Human islet graft function in NOD-SCID mice predicts clinical response in islet transplant recipients. *Transplant Proc* 36:1108–1110.
49. Stokes RA, et al. (2017) Transplantation sites for human and murine islets. *Diabetologia* 60:1961–1971.
50. Robertson RP, Lanz KJ, Sutherland DER, Kendall DM (2001) Prevention of diabetes for up to 13 years by autoislet transplantation after pancreatectomy for chronic pancreatitis. *Diabetes* 50:47–50.
51. Pagliuca FW, et al. (2014) Generation of functional human pancreatic β cells in vitro. *Cell* 159:428–439.
52. Millman JR, et al. (2016) Generation of stem cell-derived β-cells from patients with type 1 diabetes. *Nat Commun* 7:11463.
53. Anonymous (2014) First stem cell-derived islets in humans. *Nat Biotechnol* 32:959.
54. Calafiore R (2003) Alginate microcapsules for pancreatic islet cell graft immunoprotection: Struggle and progress towards the final cure for type 1 diabetes mellitus. *Expert Opin Biol Ther* 3:201–205.
55. Hentze H, et al. (2009) Teratoma formation by human embryonic stem cells: Evaluation of essential parameters for future safety studies. *Stem Cell Res (Amst)* 2: 198–210.
56. Onoe H, et al. (2013) Metre-long cell-laden microfibres exhibit tissue morphologies and functions. *Nat Mater* 12:584–590.
57. Raof NA, Padgen MR, Gracias AR, Bergkvist M, Xie Y (2011) One-dimensional self-assembly of mouse embryonic stem cells using an array of hydrogel microstrands. *Biomaterials* 32:4498–4505.
58. Lee KH, Shin SJ, Park Y, Lee SH (2009) Synthesis of cell-laden alginate hollow fibers using microfluidic chips and microvascularized tissue-engineering applications. *Small* 5:1264–1268.
59. Zhang S, et al. (2014) Creating polymer hydrogel microfibres with internal alignment via electrical and mechanical stretching. *Biomaterials* 35:3243–3251.
60. Yu Y, et al. (2014) Flexible fabrication of biomimetic bamboo-like hybrid microfibers. *Adv Mater* 26:2494–2499.
61. An D, et al. (2015) Developing robust, hydrogel-based, nanofiber-enabled encapsulation devices (NEEDs) for cell therapies. *Biomaterials* 37:40–48.
62. Lacy PE, Kostianovsky M (1967) Method for the isolation of intact islets of Langerhans from the rat pancreas. *Diabetes* 16:35–39.
63. Efron B (1982) *The Jackknife, the Bootstrap and Other Resampling Plans* (Society for Industrial and Applied Mathematics, Philadelphia).

Supporting Information

An et al. 10.1073/pnas.1708806115

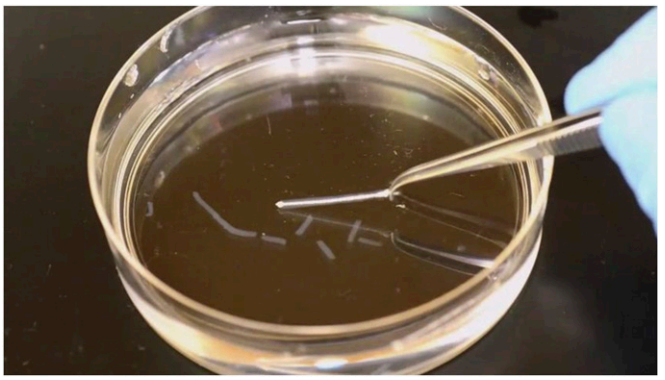

Movie S1. Handling of the TRAFFIC and neat alginate hydrogel fibers.

Movie S1

Movie S2. Retrieval of the neat alginate hydrogel fiber from the mouse peritoneal cavity.

Movie S2

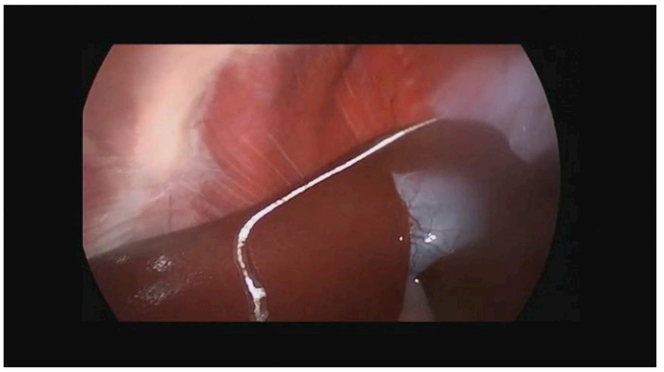

Movie S3. A laparoscopic view of the TRAFFIC sitting on the liver, 1 mo after implantation in a dog.

Movie S3

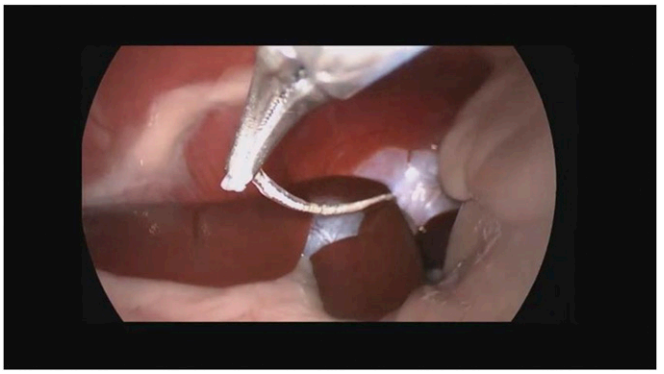

Movie S4. Laparoscopic video showing the retrieval of the TRAFFIC after 1 mo of implantation in a dog.

Movie S4

Movie S5. Digital video showing the retrieval of the TRAFFIC after 1 mo of implantation in a dog.

Movie S5

Other Supporting Information Files

SI Appendix (PDF)

SI Appendix

SI-1. Theoretical analysis of the wettability on a single smooth thread (or fiber) or twisted threads

Liquids tend to minimize their surface area by virtue of surface tension, which may cause liquid instability and fluid break-up. Sphere is the geometric shape that has the minimum surface area at a given volume, so small quantities of liquids will evolve into sphere-like droplets to reduce surface energy. In the case of a solid fiber coated with a uniform liquid film, tiny perturbations are always present and introduce the liquid instability. The instability will cause the liquid film to undulate and eventually break up into a string of droplets. The influence of gravity is neglected in this study, when Bond number that compares the importance of gravity and capillary forces approaches zero up to fiber radius of 50 μm (1).

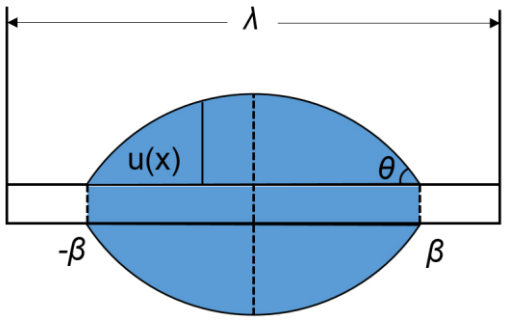

Figure S1. Diagram of a liquid droplet on a fiber (Barrel shape)

It has been reported that the liquid films coated on fibers become unstable when the wavelength λ exceeds the circumference of the liquid cylinder l (1). Here, l is expressed as $2\pi(R+t)$, where t is the film thickness and R is the fiber radius. The wavelength is given by $2\sqrt{2}\pi R$ when the liquid films are very thin (1). Thus, we have the maximum thickness of thin unstable films t_{max}, viz.

$$t_{max} = \left(\sqrt{2}-1\right)R \qquad [1]$$

When the film thickness is comparable to or greater than the fiber radius, the wavelength is found to be $2\sqrt{2}\pi(R+t)$ theoretically and experimentally (2).

The original thickness of the liquid film t_o is important to the liquid instability or the fluid break-up. Based on mass conservation, the value of t_o can be inversely determined by the final volume and shape of the droplet when liquid loss due to evaporation is negligible. In Fig. S1, the volume of the droplet V_f within one wavelength is given by

$$V_f = \pi \int_{-\beta}^{\beta} [u(x)+R]^2 dx - 2\pi R^2 \beta \qquad [2]$$

where β is the half-length of the droplet and $u(x)$ is the droplet thickness in x-direction. The original film thickness t_o is then obtained by solving the following equation,

$$\pi\lambda[(t_o + R)^2 - R^2] = V_f \quad [3]$$

It is observed that the original film thickness is comparable to the fiber radius and we have $\lambda > l$ accounting for the instability of liquid films. Then the liquid cylinder undulates and the higher pressure in the trough section drives the liquid to the peak area with lower pressure. Larger liquid droplets will be increasingly created and separated.

Twisted fibers, approximated as parallel fibers in a very short length, can reduce liquid instability and fluid break-up (see Fig. S2). The liquid meniscus in the wedges between fibers are always concave and stable, accounting for the existence of continuous liquid films along the twisted fibers. Even if liquid film undulates, thicker film tends to move to the area of thinner film for uniform thickness due to the gradient of capillary pressure.

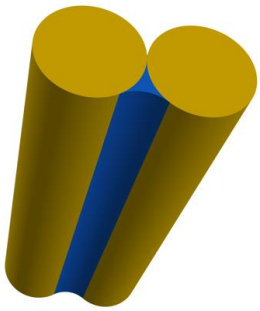

Figure S2. Liquid films inside a wedge between two tightly packed fibers

It has been shown that the liquid attached to a solid edge with dihedral angle 2α is stable when $\alpha + \theta < \pi/2$ (3). Here, $\overline{CG}$ is tangential with the fiber surface and assumed as one side of the edge, α is equivalent to $\angle PGC$, $\overline{CO}$ is the radius of the arc $\widehat{CD}$, and θ is the contact angle and has the same value with $\angle OCP$ (see Fig. S3). It is evident that the arc length of $\widehat{CE}$ is greater than the line length of $\overline{CG}$. Thus, parallel or twisted fibers favor penetration of the liquid in the wedges for uniform, continuous liquid film, when $\angle PGC + \theta < \pi/2$ or the liquid-vapor interface $\widehat{CD}$ is concave. Even with a relatively high contact angle, the continuous liquid film can be retained stably in the deeper region of the wedge with a smaller α, considering the convex surface of cylindrical fibers. In analogy, the liquid films tend to stay stably in the wedge surrounded by neighboring fibers, when more fibers are used to develop the twisted thread.

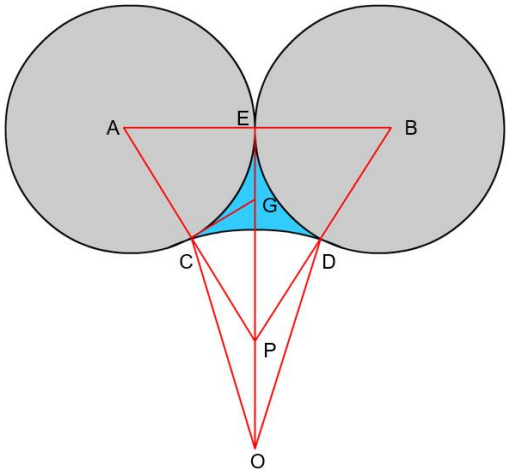

Figure S3. Cross-section view of a liquid within the wedge between two cylindrical fibers

SI-2 Experimental analysis of the wettability on a single smooth suture or twisted-folded sutures

As suggested by our theoretical analysis, the behavior of coating solution is different between the monofilament suture and the twist-folded sutures. Here we confirmed the difference experimentally. The PMMA/DMF solution formed periodical beads on the monofilament nylon suture (Fig. S4a), however, in the case of the twisted sutures, the polymer solution wetted the entire structure much more uniformly.

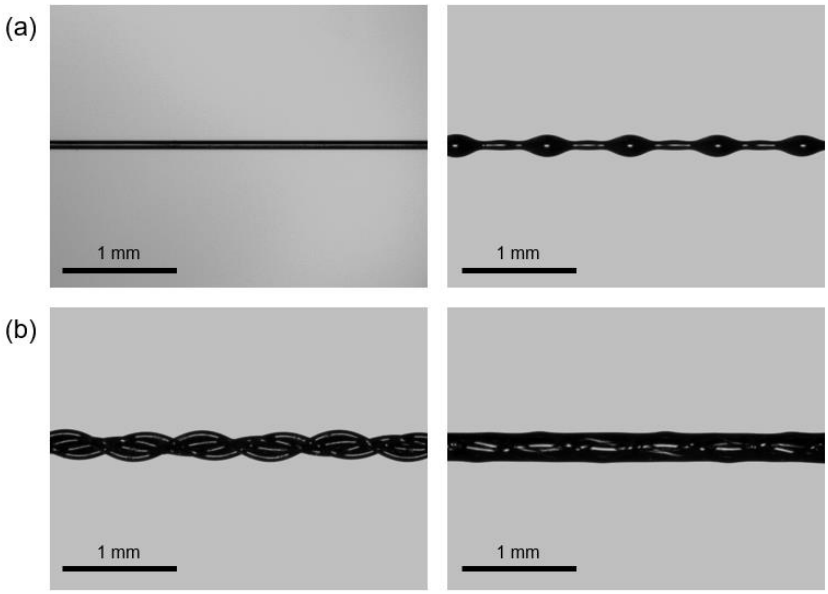

Figure S4. Goniometer photos of the PMMA/DMF solution on a monofilament Nylon suture (**a**) and twist-folded sutures (**b**). Left: before coating; right: after coating.

The different wetting behavior resulted in different surface coatings on the sutures. The polymer solution on the monofilament suture was dried into periodical beads, i.e. “beads-on-a-string” structure (Fig. S5a). On the other hand, the polymer coating on the twisted sutures was much more uniform (Fig. S5b).

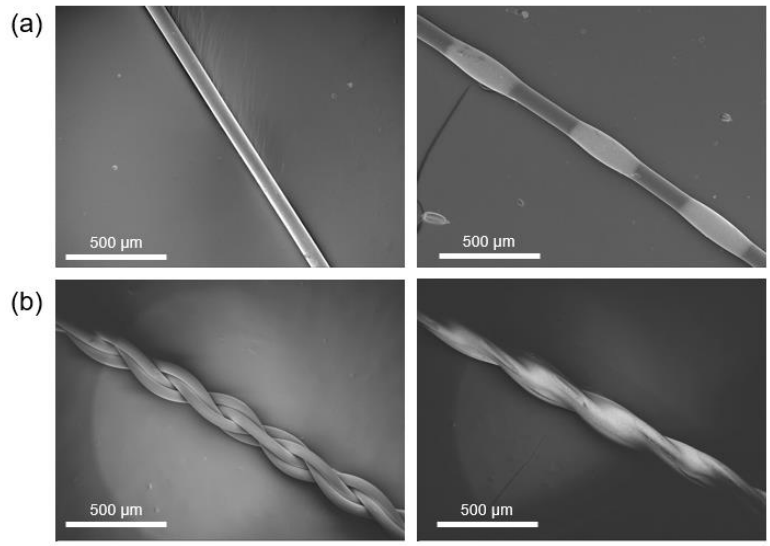

Figure S5. SEM images of the polymer coated sutures. **a**, "beads-on-a-string" coating on a monofilament. **b**, Uniform coating on "ridges-in-grooves" structure. Left: before coating; right: after coating.

The different uniformity of the polymer coatings also led to a difference in the calcium ion distribution, which sometimes could affect the uniformity of the *in situ* crosslinking of alginate hydrogel. As shown in Fig. S6a, EDX element mapping images show the periodical distribution of the $CaCl_2$ distribution. In this case, the uniformity of the alginate hydrogel layer was less well controlled. (Fig. S6b).

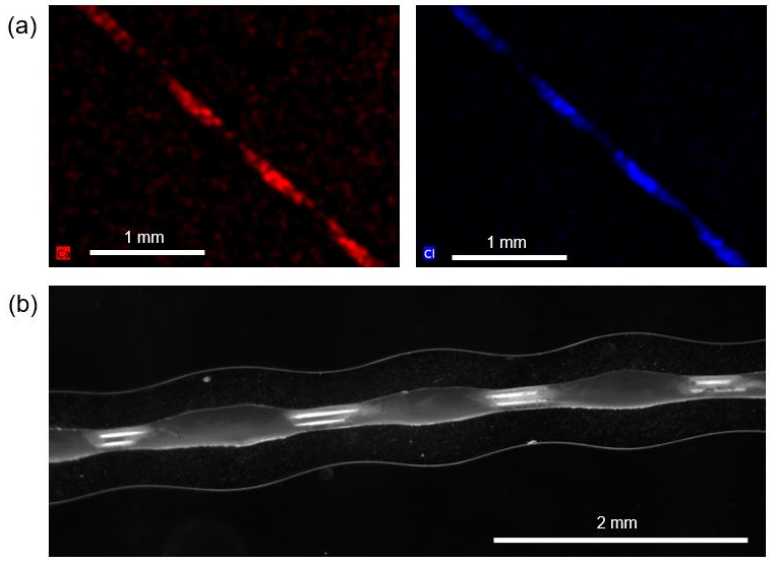

Figure S6. **a**, EDS element mapping of the beaded fiber. **b**, A microscopic image showing the non-uniform thickness of the hydrogel coating.

SI-3 Thickness control of the device

The hydrogel thickness can be easily controlled by various methods. For example, the diameter of the device can be tuned by varying the $CaCl_2$ concentration in the surface modification or the submerging time in alginate solution. As shown in Fig. S7a, using the same size (~150 μm) suture, the hydrogel layer thickness can be tuned from 500 μm to 1.3 mm by controlling these two parameters (Fig. S7b).

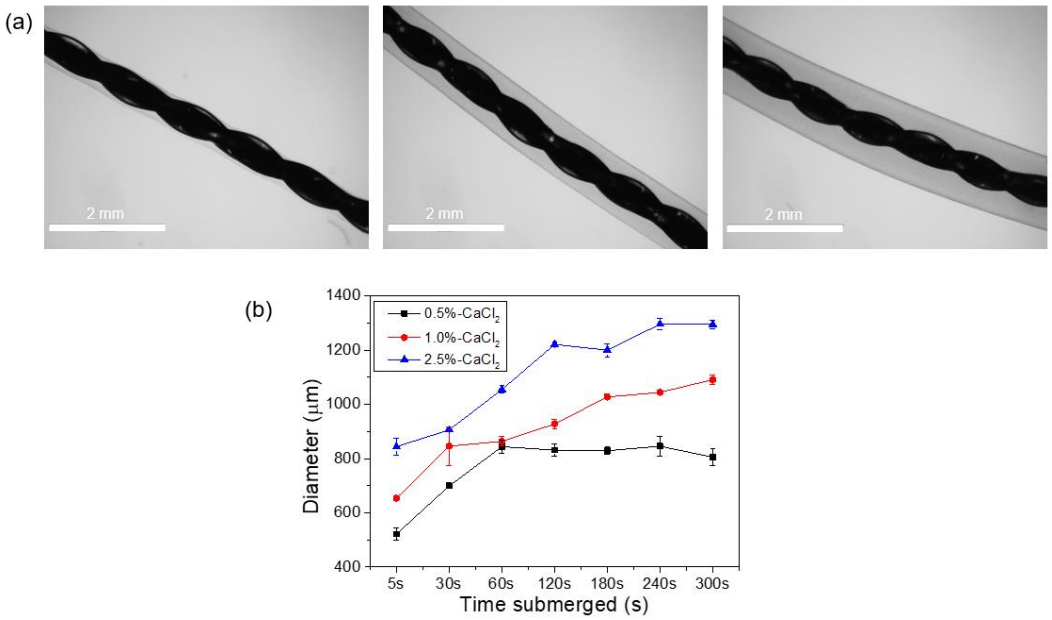

Figure S7. Control of hydrogel thickness by changing the $CaCl_2$ concentration in the coating solution or the crosslinking time in alginate solution. **a**, Representative images of the TRAFFIC devices with different hydrogel thicknesses. **b**, The diameters of the device as a function of $CaCl_2$ concentration and crosslinking time.

Smaller or larger diameters of the devices can be achieved by using twisted sutures of different sizes. (Fig. S8)

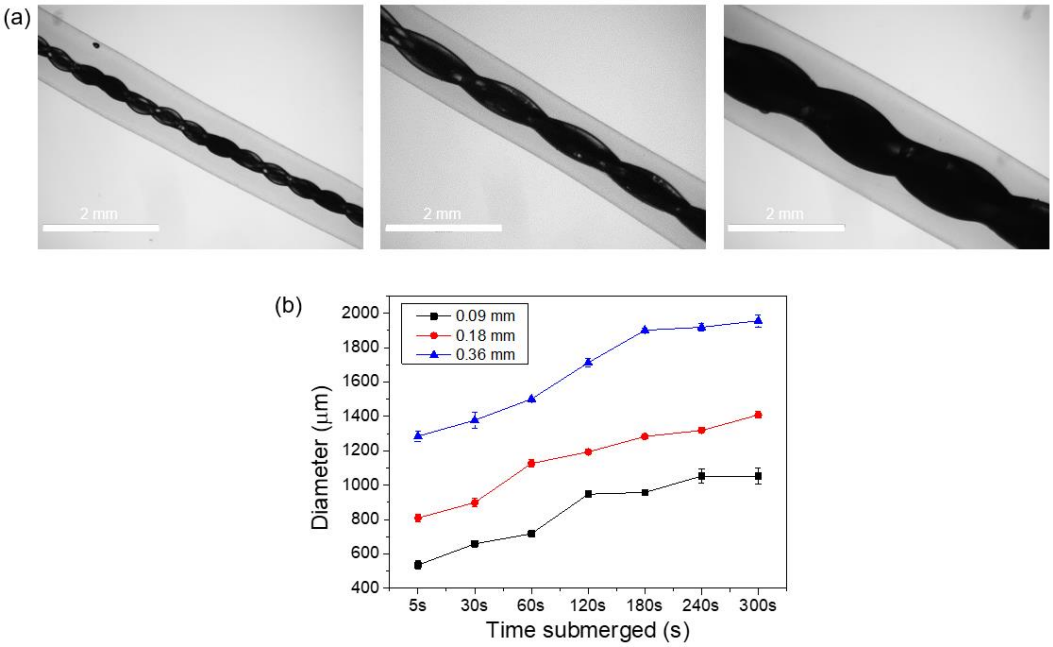

Figure S8. Control of hydrogel thickness by using different size sutures and tuning the crosslinking time in alginate solution. **a**, Representative images of the TRAFFIC devices with different sizes of twisted sutures. **b**, Calibration curve of the TRAFFIC diameters, with the legend indicating the diameter of each monofilament suture.

SI-4 Comparison with the sequential dipping method

Coating a thread with alginate hydrogel may also be achieved by a sequential dipping method (Fig. S9a) (4). However, the coating was much less well controlled and it often resulted in much less uniform hydrogel thickness. For example, when we dipped a commercially available nylon suture strand sequentially into $CaCl_2$ buffer, alginate solution, and $CaCl_2$ buffer again, the resulting alginate coating was far from uniform (Fig. S9b). The non-uniformity would likely impair the stability of the device since the thinner part of the hydrogel coating would likely break first and cause a leak of the encapsulated cells. In contrast, our method, due to the continuous nanoporous, $CaCl_2$-releasing coating, leads to controllable and uniform hydrogel formation around the thread (Fig. S9c).

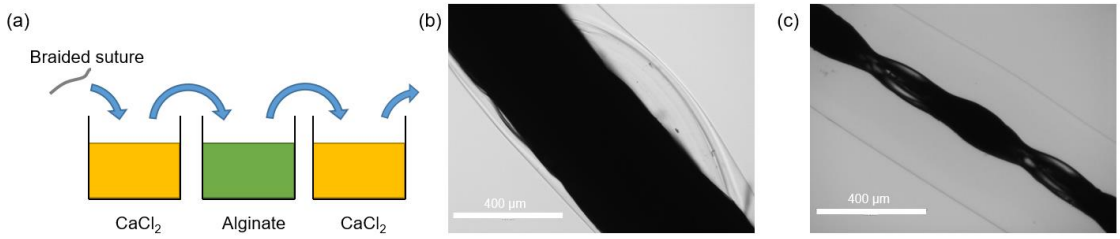

Figure S9. Comparison with the sequential dipping method. **a**, Schematic illustration of a sequential dipping method. **b**, Microscopic image showing the non-uniform alginate hydrogel coating. **c**, Microscopic image showing the uniform hydrogel formation using the *in situ* crosslinking method described in this work.

SI-5 Discussion on the hydrogel-thread adhesion

Mechanical robustness is one of the most important features of any implantable/retrievable biomedical device. Alginate hydrogel fiber is usually very weak and brittle; it could easily break during implantation or inside the body. Especially when therapeutic cells derived from stem cells are used, the retrievability and mechanical robustness are highly desired to mitigate the concerns of teratoma formation.

To enhance the mechanical property of an alginate hydrogel fiber, we need both a tough thread and a strong adhesion between the thread and the hydrogel. To quantitatively characterize the effective adhesion of the thread and the hydrogel, we measured the forces required to pull the thread out of the hydrogel in three different cases (Fig. 2b in main text): devices made from bare monofilament suture, "beads-on-a-string" thread and the twisted, continuously modified thread. To perform the measurement, we used a Dynamic Mechanical Analysis (DMA Q800) instrument to pull the thread with an increasing load at 0.1 N/s until it reached a threshold at which point the load dropped by 20% sensitivity value. The load-displacement curves shown in Fig.2b in the main text indicate that the twisted thread had the strongest adhesion with the alginate hydrogel.

There are three key factors that affect the mechanical stability of the hydrogel-reinforcement composite: the intrinsic adhesion between the hydrogel and the reinforcement thread, the interfacial area between the nanoporous surface and the hydrogel, and the macroscopic structure of the reinforcement thread. In order to investigate how these factors influence the composite toughness, we conducted finite element simulations of the fiber pullout for both the beaded thread and the twisted thread geometry. The gel was modeled as linear elastic. The thread which is ~100,000 times stiffer than the gel was modeled as rigid. Since the adhesion of the gel is unknown, we simulated two extreme cases: no adhesion and perfect bonding. We found that for the case of no adhesion, the beaded geometry has a much higher pullout force-to-displacement ratio. In this scenario the resistance to pullout comes from the gel having to deform around the thread as the thread moves through. The beaded geometry provides more of an obstacle than the twisted thread geometry. While this no adhesion geometry effect is interesting, it does not correlate with the experimentally observed trends or force magnitudes. When the pullout is simulated with strong adhesion, the force-to-displacement ratio for both systems goes up many orders of magnitude, implying that adhesion is paramount for the composite toughness. Further, the twisted thread geometry has a moderately higher (~25%) force-to-displacement ratio than the beaded geometry. Given that the adhesion from the infiltrated nanoporous surface seems to be large, we also looked at stress distribution within the gel to examine susceptibility of fracture within the gel rather than failure at the gel-thread interface. In Fig. S10 we show a cross-sectional view of the hydrostatic pressure in the gel for the two systems at the same pulling force (thread removed from image). The beaded geometry has a mild stress concentration at the vertical edge of the beads, suggesting a higher susceptibility to gel cavitation than in the twisted thread case.

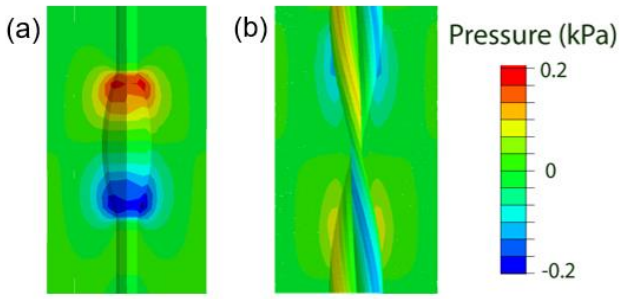

Figure S10. Hydrostatic pressure within the gel resulting from vertical displacement of the thread while holding the gel edge fixed (cross-sectional view): “beads-on-a-string” thread (**a**) and twisted thread (**b**).

SI-6 Mechanical stability comparison between neat alginate fiber and TRAFFIC device

Empty TRAFFIC devices and neat alginate hydrogel fiber with the same length and diameter were implanted into C57BL/6 mice intraperitoneally. After one week, the intraperitoneal cavity was opened to retrieve the implant. As shown in Fig. S11, the TRAFFIC device remained its shape, however, the neat alginate hydrogel fiber folded and entangled with itself and caused some tissue adhesion.

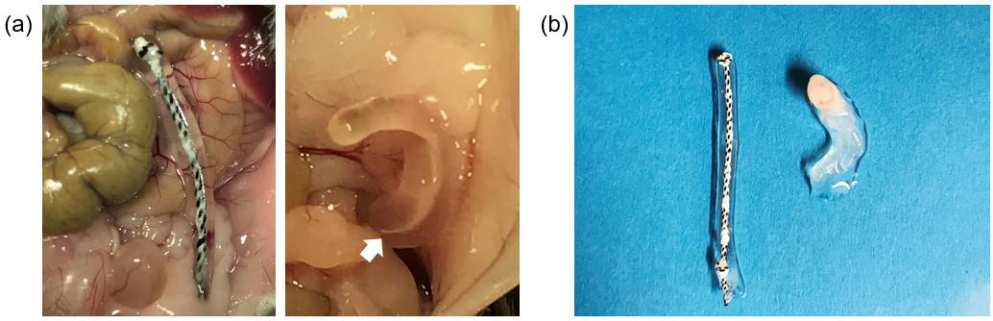

Figure S11. *In vivo* mechanical stability test. **a**, digital images of a TRAFFIC device (left panel) and a neat alginate hydrogel fiber (right) during retrieval, with the arrow indicating the entangled region. **b**, digital images of the retrieved TRAFFIC device and the neat alginate hydrogel fiber.

SI-7 Optimization of biocompatibility

Fibrosis is one of the major obstacles that almost every cell encapsulation device faces. The cellular overgrowth on the surface of the cell encapsulation device impairs the mass transfer of oxygen and nutrients to encapsulated cells (5-7). Recently much progress has been made in optimizing the biocompatibility of alginate hydrogel materials. For example, it was shown that increasing the size of alginate spheres significantly reduced the fibrosis formation when they were implanted in mice and primates (8). Inspired by this study, we tested whether the size of our TRAFFIC device would play a similar role in fibrotic reaction. We first conducted a 2-week long pilot study, since it was reported that a 2-week exposure to the intraperitoneal space was sufficient to elicit fibrosis (8). We tested two groups of TRAFFIC with a length of ~1 inch and respective diameters of ~1.3 mm and ~500 µm. Interestingly, 2 weeks after intraperitoneal implantation in C57BL/6 mice, the small diameter group induced significant fibrotic reaction, while the large diameter group had much less fibrosis. (Fig. S12). This pilot study seemed to suggest the alginate spheres and TRAFFIC or essentially alginate cylinders followed a similar trend in the size effect on fibrosis. While we did not fully understand how the size affected the fibrosis here, we postulated that smaller devices could be stiffer due to the higher volume fraction of the suture thread, have a higher chance for incomplete hydrogel coverage due to the thinness, release a higher amount leachable (e.g. Ba^{2+}) due to the higher surface area per unit volume or be easier to be enveloped or trapped in a soft tissue simply because of the smaller size.

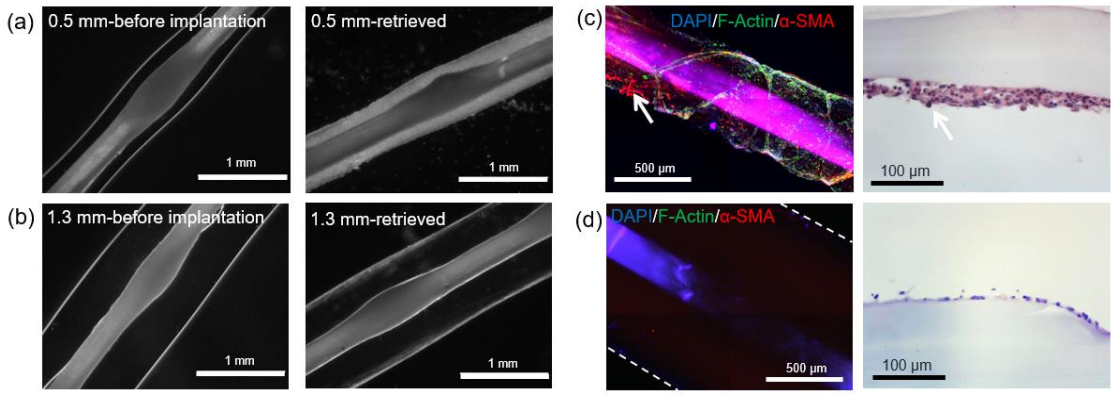

Figure S12. 2-week fibrosis study. **a**,**b**, TRAFFIC devices with diameters of 500 µm (**a**) and 1.3 mm (**b**) before and after implantation (n=5). **c**,**d**, Immunohistochemistry analysis and H&E staining of the retrieved devices with different sizes retrieved after 2 weeks: TRAFFIC with a diameter of 500 µm (**c**) and 1.3 mm (**d**) (n=5), cellular deposition was examined by immunostaining using DAPI (nucleus marker), F-actin (cellular cytoskeleton marker), and alpha-smooth muscle actin (α-SMA, myofibroblast marker).

To confirm this size effect held true for a longer implantation time, we conducted a 3-month experiment. We observed again that the devices with ~1.3 mm

in diameter had minimal cell attachment and the smaller diameter group (500 µm in diameter) were all covered by several layers of overgrown cells (Fig. S13, Fig. S14).

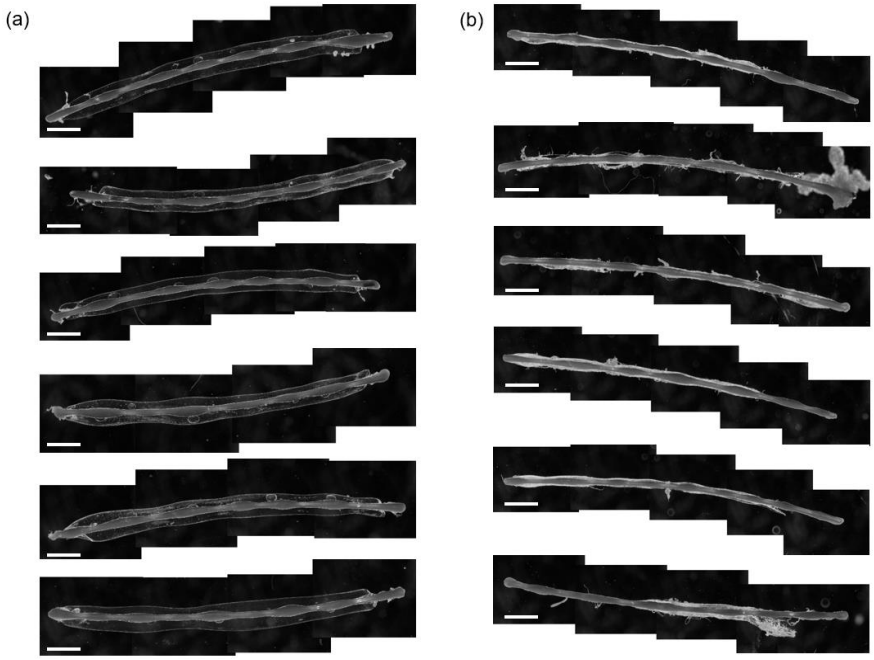

Figure S13. 3-month fibrosis study. Retrieved TRAFFIC devices with diameters of ~1.3 mm (**a**) and ~500 µm (**b**), all scale bars: 2mm.

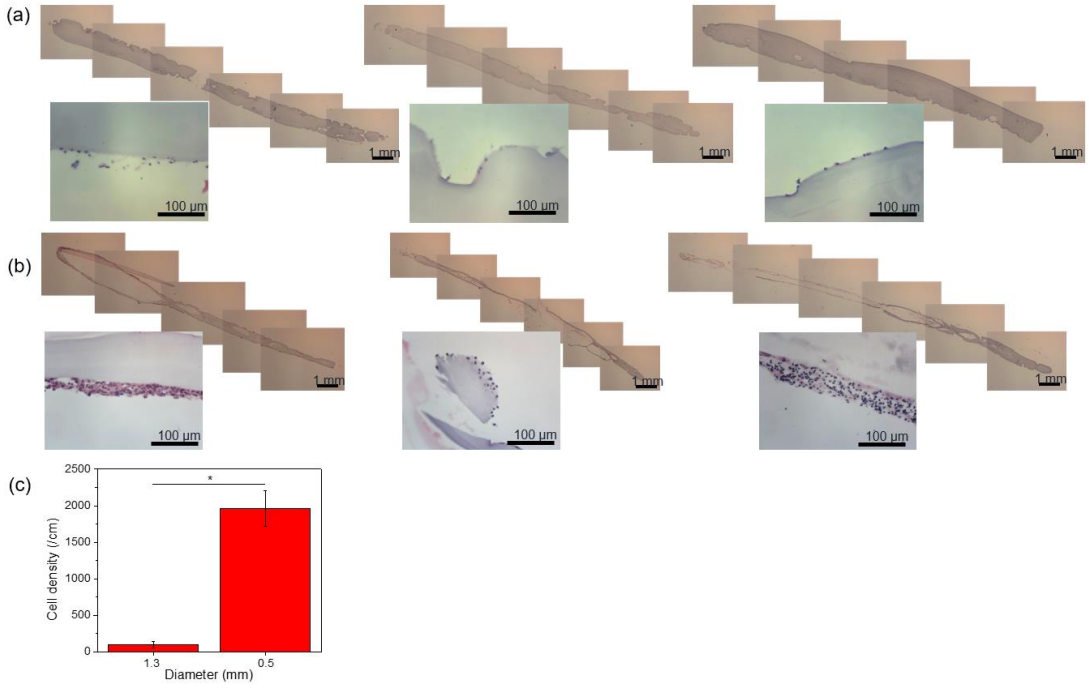

Figure S14. H&E staining of the TRAFFIC devices with different diameters of ~1.3 mm (**a**) and ~500 µm (**b**), retrieved after 3 months. **c**, A quantification of the density of attached cells, n=3, mean±s.e.m., **P*<0.05.

Encouraged by the results from the size effect studies, we further tested the biocompatibility of optimized TRAFFIC device (i.e. with a diameter of ~1.3 mm) over an even longer time implantation. Eleven empty devices were implanted into 11 healthy C57BL/6 mice. After 7 months, the devices were retrieved and examined. Ten out of the eleven devices had no tissue adhesion or significant fibrosis (Figs. S15, S16). Histology images also confirmed the minimal cell attachment on the devices (Fig. S17).

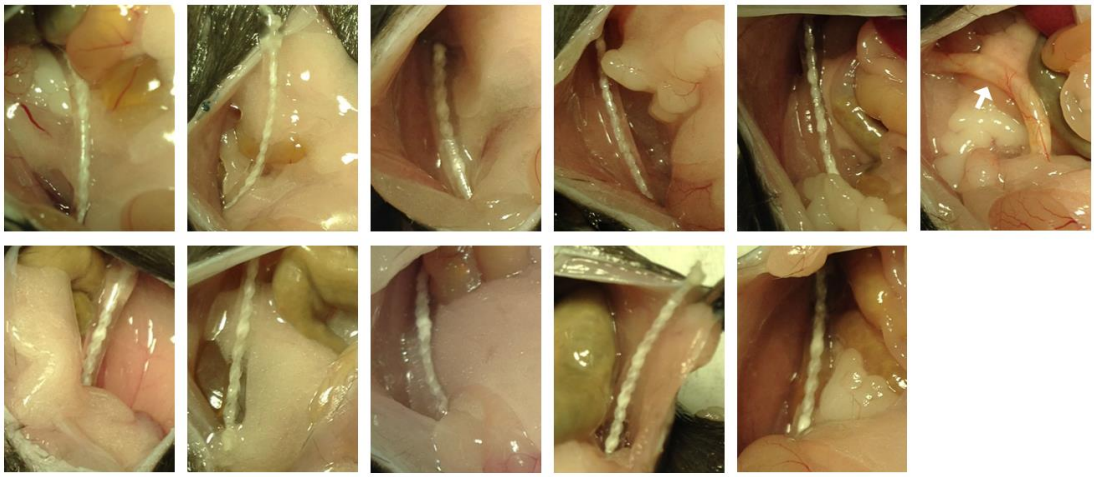

Figure S15. Digital images showing the devices with a diameter of ~1.3 mm implanted in the intraperitoneal space of mice for 7 months. (The arrow points to a device that caused severe fibrotic reaction.)

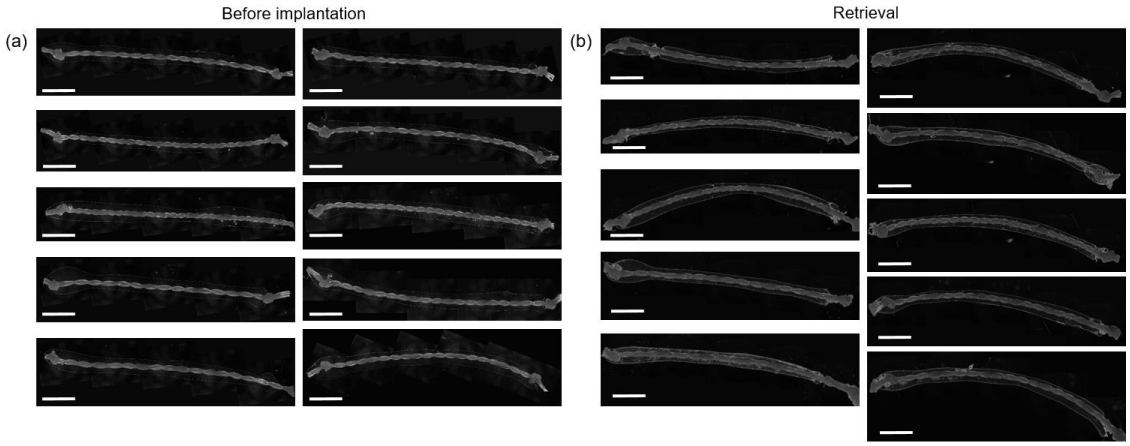

Figure. S16. Microscopic images of the devices before (**a**) and after (**b**) 7-month implantation, all scale bars: 2mm. (The one with severe fibrosis could not be imaged and is not shown here.)

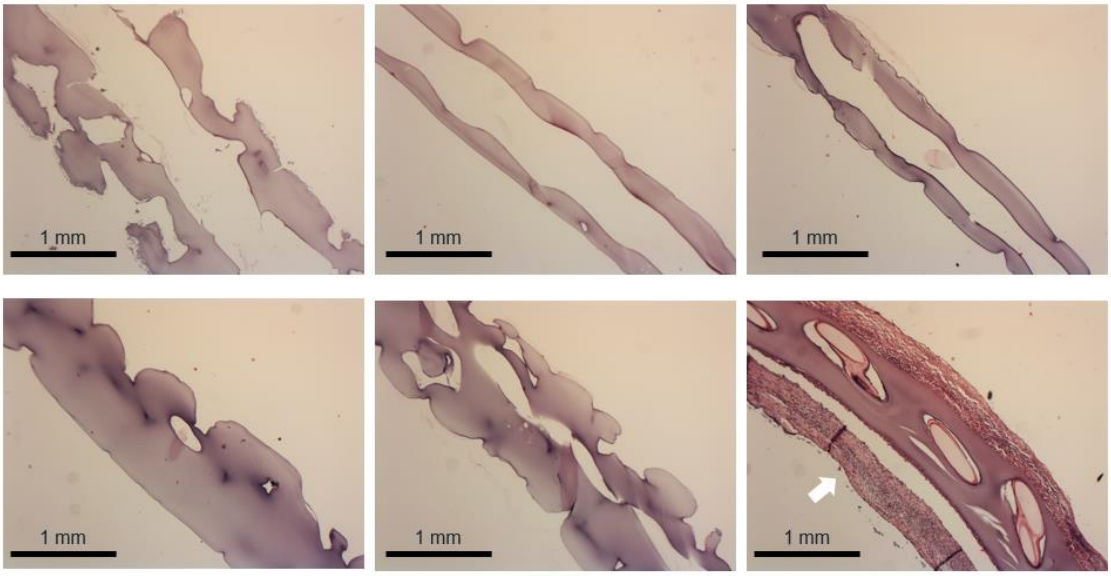

Figure. S17. H&E staining of the devices retrieved after 7-month implantation. (6 of the 11 devices were analyzed histologically; the arrow in last image points to the thick fibrotic layer for one of the devices.)

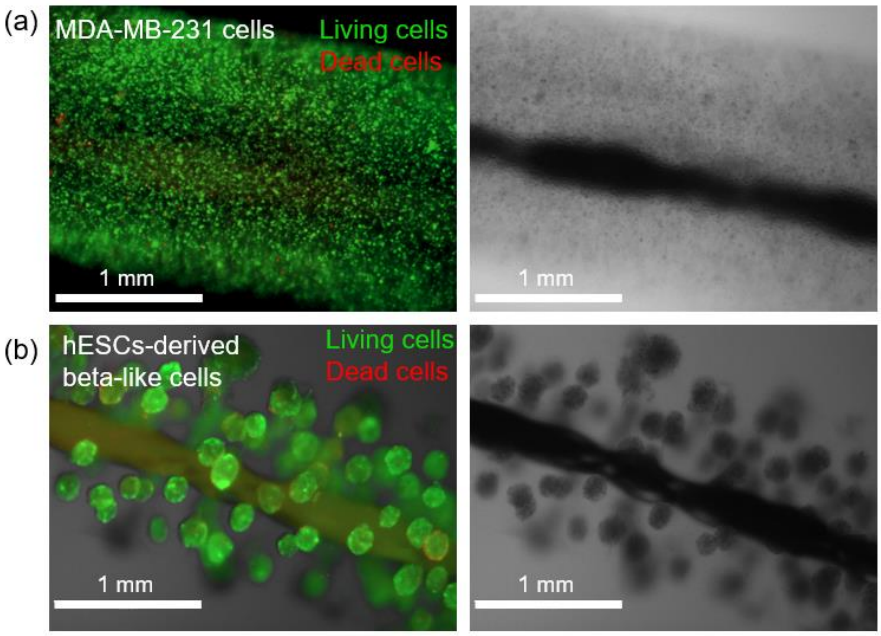

Figure S18. Encapsulation of other types of cells. **a**, Live (green) /dead (red) staining of MDA-MB-231 cells encapsulated in the device after a 4-day culture. **b**, Live/dead staining of aggregates of human Embryonic Stem Cell (hESC)-derived beta-like cells encapsulated in the device after a 3-day culture.

SI-8 Permeability measurement

To assess the semi-permeability of the TRAFFIC, we immersed the TRAFFIC in four different saline solutions containing 10 kDa, 70 kDa, 250 kDa and 500 kDa FITC-labeled dextrans, respectively. The fluorescent intensity of the TRAFFIC was analyzed using confocal microscopy (Fig. S19). The results indicated that the alginate hydrogel used in TRAFFIC would prevent diffusion of molecules above 250kDa.

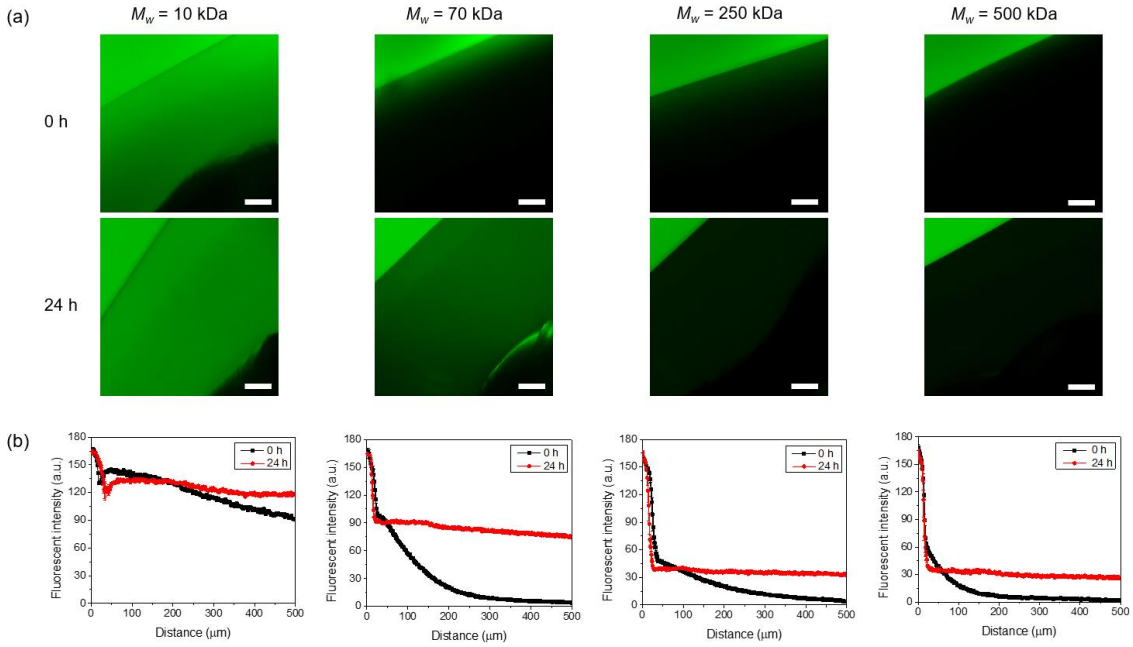

Figure S19. Permeability measurement of the TRAFFIC. Fluorescent images (**a**) and intensity profiles (**b**) showing the permeability of TRAFFIC devices to different molecular weight FITC-dextrans. The TRAFFIC devices were immersed in saline solutions containing FITC-dextrans with four molecular weight (M_w=10,000, 70,000, 250,000, and 500,000), all scale bars: 100 μm.

SI-9 Comparison of rat islets encapsulated in TRAFFIC, rat islets encapsulated in neat alginate fiber and BALB/c mouse islets encapsulated in TRAFFIC

To further test the performance of the TRAFFIC device, we included control groups of rat islets encapsulated in neat alginate fiber and BALB/c mouse islets encapsulated in TRAFFIC. Here, the same amount of rat islets (~475±25 IEQ) was encapsulated in both TRAFFIC devices and neat alginate fibers of similar dimensions; a smaller amount of islets (~380±20 IEQ) isolated from BALB/c mice was encapsulated in TRAFFIC. These encapsulated islets were transplanted into diabetic C57BL/6 mice. As shown in Fig. 3h in the main text, the blood glucose concentrations of all three groups dropped into a normal range after transplantation. The normoglycemia was maintained for about one month before retrieval. The body weight of the diabetic mice gradually increased after transplantation (Fig. S20a). The IPGTT (28 days after transplantation) of the diabetic mice showed no significant difference among the different transplantation groups (Fig. S20b). We characterized the retrieved islets using optical microscopy (Fig. S20c), live/dead staining (Fig. S20d), immunohistochemistry and H&E staining (Fig. S20e). The results showed viability and function of the retrieved islets from all three groups.

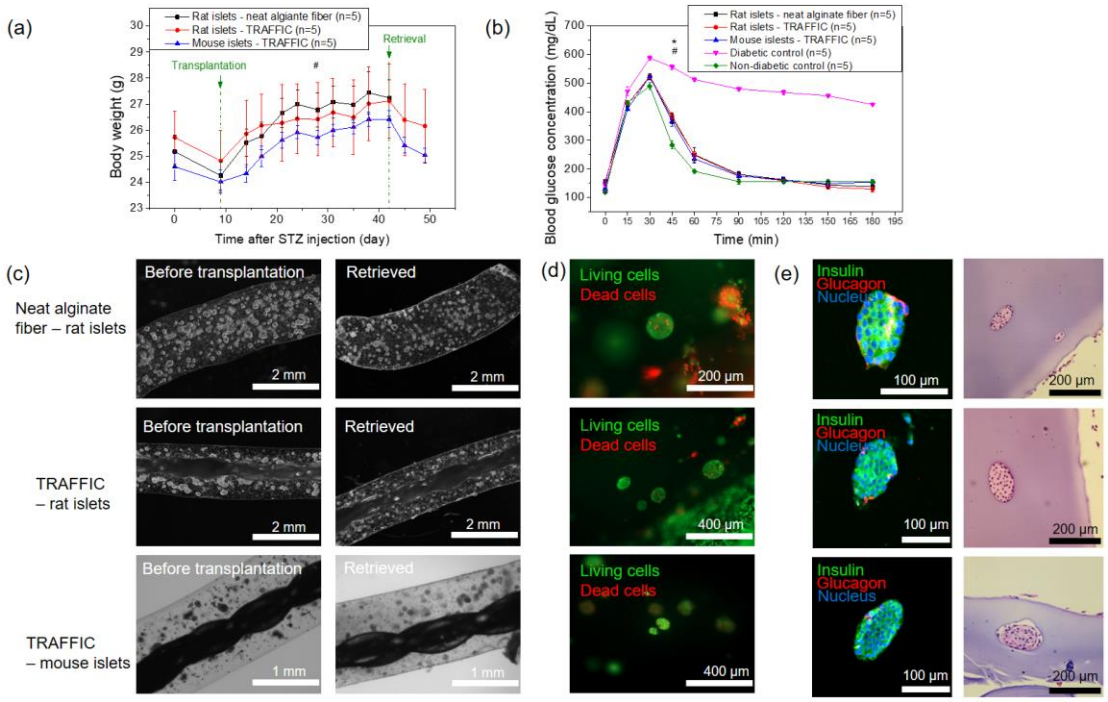

Figure S20. Transplantation of rat islets encapsulated in neat alginate fiber or TRAFFIC and allogenic mouse islets encapsulated in TRAFFIC. **a**, Body weight of the C57BL/6 diabetic mice after transplantation, n=5, mean±s.e.m., #P>0.05 (among all three groups). **b**, Intraperitoneal glucose tolerance test prior to retrieval on day 28, n=5, mean±s.e.m., *P<0.05 (three groups with transplantations versus the diabetic control), #P>0.05 (among the three groups with transplantations). **c**, Optical microscope images of the device/islets before transplantation and after retrieval. **d**,

Live/dead staining of the retrieved islets. **e**, Immunohistochemical staining and H&E staining of the retrieved islets.

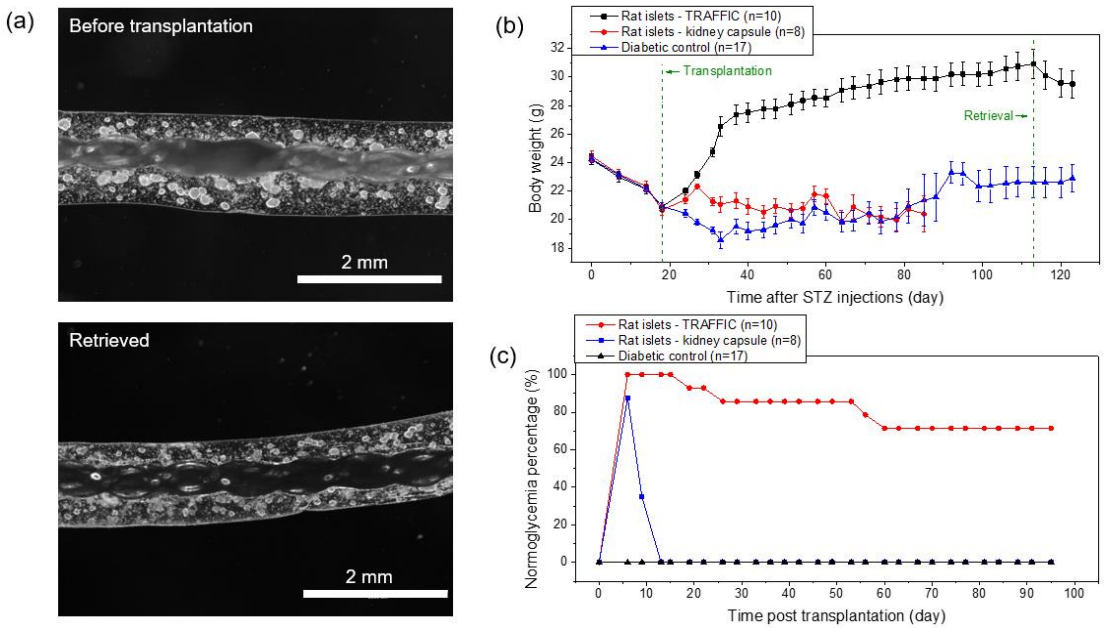

Figure S21. a, Optical microscopic images of the rat islets in TRAFFIC before transplantation and retrieved after 3 months. **b**, Body weight of the C57BL/6 diabetic mice that received transplantation of rat islets. **c**, Percentage of cured mice for different groups.

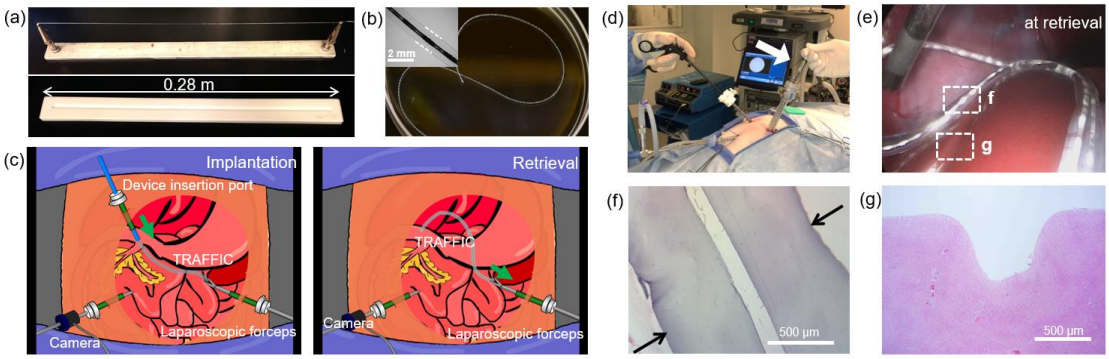

Figure S22. a, A digital image of custom-made tools for fabrication of long TRAFFIC. **b**, A digital image of a ~10-inch-long empty device for canine implantation, inset: a microscopic image of the device. **c**, **d**, Schematic illustrations and a digital image showing the laparoscopic procedures; the arrow in **(d)** indicates the insertion of the device into a dog during intraperitoneal implantation. **e**, Laparoscopic image of the device 2 weeks after implantation. **f**, H&E staining of the retrieved device. **g**, H&E staining of the liver tissue in contact with the device.

SI-10 Scale-up of the device

In our design, the device can be easily scaled up longitudinally. As shown in Fig. S23a, a string holder and a trough both of ~0.28 m in length were used to fabricate a typical device for the dog experiments. The system may be further scaled up using channel reservoirs such as the one shown in Fig. S23a. Moreover, due to the excellent mechanical stability and the flexibility, the long devices can be tied together and folded in order to fit into the laparoscopic trocar (Fig. 23b, c). We estimate if we increase further the diameter of the device and reach an encapsulation density of ~4,000 islets per inch, we would need 8 arms of ~12.5-inch TRAFFIC which in principle is still feasible to cure a human patient.

Figure S23. Scale-up of the device. **a**, Trough capable of fabricating a device of ~2.24 m. **b**, Device with 4 arms tied together with a total length of ~0.7 m. **c**, The knot region of the tied device.

SI-11 Laparoscopic implantation procedure

To use laparoscopy to implant the device, we first fit the device into a 2 mL sterile pipette (Fig. S24a). The anesthetized dog's abdomen was insufflated to 12 mm Hg pressure with CO_2. Three laparoscopic ports were percutaneously inserted into the abdomen, one for the camera, one for device insertion, and one for laparoscopic probe/forceps (Fig. S24b). Once the device was inserted and placed in the abdomen, the ports were removed and the incisions closed using sutures (Fig. S24c). Fig. S24d shows the healed incisions after 1 month.

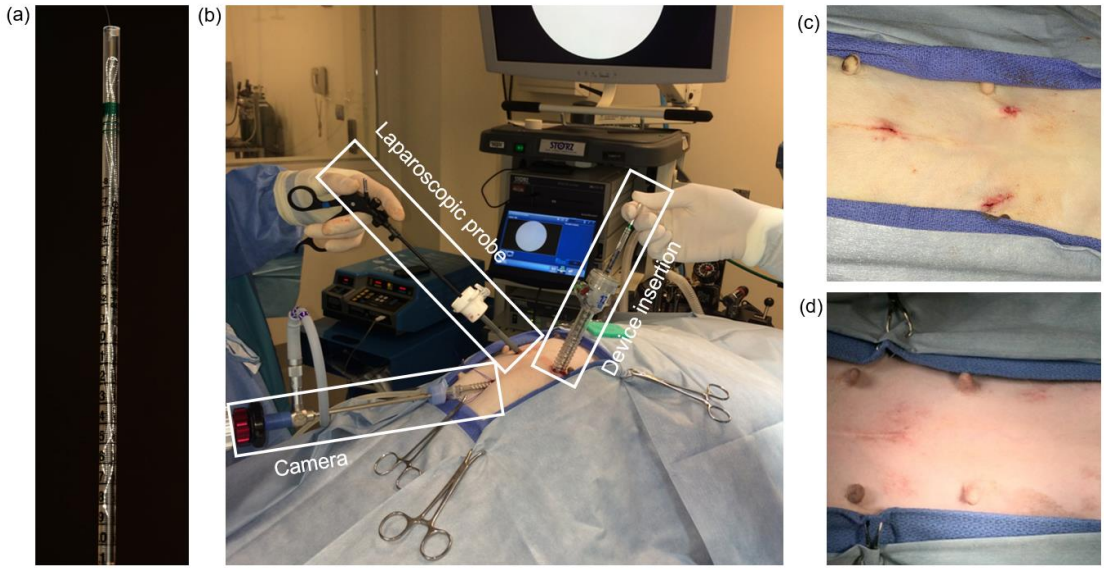

Figure S24. Laparoscopic implantation procedure. **a**, Device folded into a 2 mL pipette. **b**, Digital image of the laparoscopic implantation set-up. **c**, The three sutured incisions right after the implantation. **d**, Photograph showing healing of the incisions after 1 month.

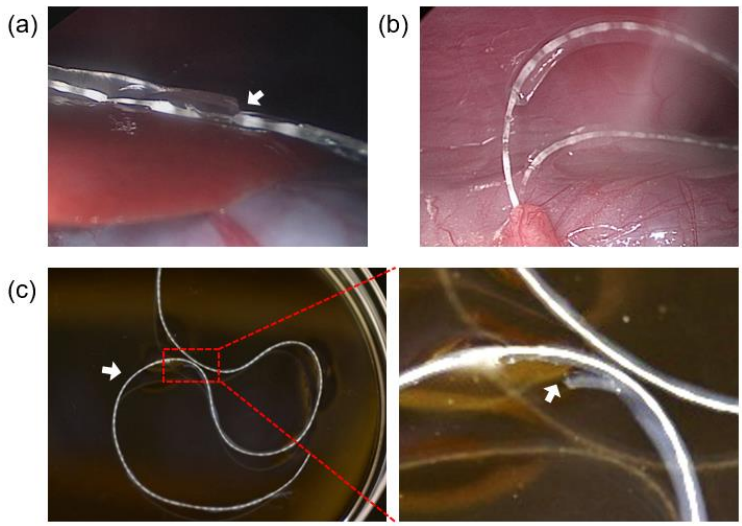

Figure S25.Weak mechanical stability of the device made from a "beads-on-a-string" thread. **a**, A laparoscopic image showing the alginate hydrogel partially detached in the peritoneal space of a dog. **b**, Laparoscopic image showing tissue adhesion of the exposed thread where the alginate hydrogel detached. **c**, Digital images showing a detached part of the retrieved device.

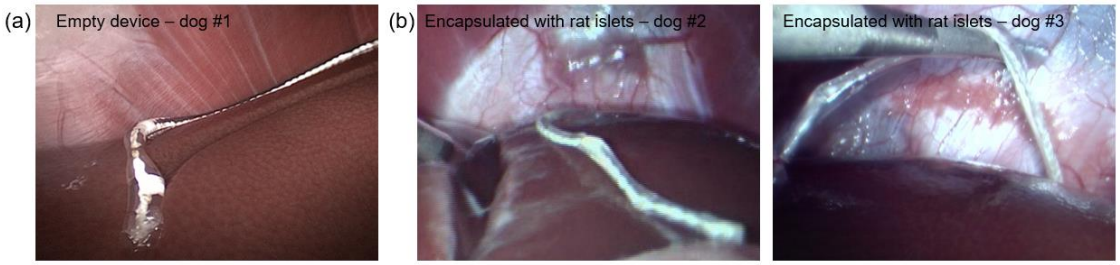

Figure S26. Additional dog implantation/transplantation data. **a**, Laparoscopic image showing an empty device above the liver after 1-month implantation. **b**, laparoscopic images showing the rat islets encapsulated devices above the dogs' livers after 1-month transplantation, arrow indicating possible inflammation on the liver.

Supplementary references

1. Quéré D (1999) Fluid coating on a fiber. *Annu. Rev. Fluid Mech.* 31(1):347-384.
2. Haefner S*, et al.* (2015) Influence of slip on the Plateau-Rayleigh instability on a fibre. *Nat. Commun.* 6:7409.
3. Langbein D (1990) The shape and stability of liquid menisci at solid edges. *J. Fluid Mech.* 213:251-265.
4. Akbari M*, et al.* (2014) Composite Living Fibers for Creating Tissue Constructs Using Textile Techniques. *Adv. Funct. Mater.* 24(26):4060-4067.
5. Desai T & Shea LD (2017) Advances in islet encapsulation technologies. *Nat. Rev. Drug Discov.* 16:338–350.
6. Bray N (2016) Modified alginates provide a long-term disguise against the foreign body response. *Nat. Rev. Drug Discov.* 15(3):1.
7. Krishnan R, Alexander M, Robles L, Foster 3rd CE, & Lakey JR (2014) Islet and stem cell encapsulation for clinical transplantation. *Rev. Diabet. Stud.* 11(1):84.
8. Veiseh O*, et al.* (2015) Size- and shape-dependent foreign body immune response to materials implanted in rodents and non-human primates. *Nat. Mater.* 14(6):643-651.